Climate Modes~~Variabilities~~ Synergistically Influence Marine Heatwaves in the North Sea

Yuxin Lin[1,2], Zhiqiang Liu[1,3*], Feng Zhou[4,5], Qicheng Meng[4,5], Wenyan Zhang[2*]

[1]Department of Ocean Science and Engineering, Southern University of Science and Technology, Shenzhen, China
[2]Institute of Coastal Systems—Analysis and Modeling, Helmholtz-Zentrum Hereon, Geesthacht, Germany.
[3]Center for Complex Flows and Soft Matter Research, Southern University of Science and Technology, Shenzhen, China
[4]State Key Laboratory of Satellite Ocean Environment Dynamics, Second Institute of Oceanography, Ministry of Natural Resources, Hangzhou, China
[5]Observation and Research Station of Yangtze River Delta Marine Ecosystems, Ministry of Natural Resources, Zhoushan, China

Correspondence to: Wenyan Zhang (wenyan.zhang@hereon.de), Zhiqiang Liu (liuzq@sustech.edu.cn)

Abstract

Global shelf seas have experienced unprecedented marine heatwaves (MHWs) in recent decades. Although ~~marine heatwaves~~MHWs have been extensively studied at the global scale, their regional variability and underlying mechanisms remain poorly understood, particularly in shelf seas influenced by multiple climate modes. ~~Although state-of-the-art forecast systems show skilful prediction of MHWs in tropical regions, their limited performance elsewhere highlights the need for a more complete mechanistic understanding at regional scales.~~ Here, we examine MHW variability ~~MHWs in~~in the Northeastern Atlantic shelf~~, a region strongly influenced by multiple large-scale climate modes~~~~climate variabilities~~~~climate modes. U~~ using a correlation-based k-means clustering approach~~, ~~. Two distinct subregions with contrasting seasonal patterns are identified~~we identified two distinct subregions with contrasting seasonal patterns~~. In winter, the southern North Sea ~~(Cluster 1)~~ experiences increased MHW frequency, intensity, and duration. This enhancement is linked to a positive East Atlantic Pattern, which ~~typically develops following a negative North Atlantic Oscillation in late autumn.~~~~The southern North Sea (Cluster 1) exhibits increased MHW frequency, intensity, and duration in winter, primarily associated with a positive East Atlantic Pattern that typically follows a negative North Atlantic Oscillation in late autumn.~~ ~~These conditions~~ intensif~~y~~ies westerly winds and enhances warm Atlantic inflow through both atmospheric and oceanic pathways. In contrast, the northern North Sea ~~(Cluster 2)~~ shows enhanced MHW frequency and duration in summer, while MHW intensity weakens.~~,~~ ~~driven by teleconnections across multiple ocean basins.~~ This summer response is modulated by ~~The~~ Atlantic Multidecadal Variability ~~modulates these linkages~~, with its positive phase strengthening Pacific-Atlantic connections via Rossby wave propagation, altering cloud cover and surface radiative forcing.~~.~~ A shallow mixed layer, enhanced stratification, and circulation-induced upwelling favor frequent and persistent but less intense summer MHWs. This north-south contrast demonstrates that different combinations of atmospheric and oceanic processes shape MHW variability across the shelf, providing a diagnostic and mechanistic framework for understanding regional MHW variability and its potential predictability.~~providing a physical basis for improving regional MHW prediction.~~

1 Introduction

Marine heatwaves (MHWs), defined as anomalous warm seawater events (Pearce et al., 2011)~~.~~, have become more frequent, persistent, and intense over the past decades, with persistent temperature extremes significantly affecting marine ecosystems and commercial fisheries (Yan et al., 2020). These trends are largely attributed to anthropogenic global warming (Mohamed et al., 2024; Oliver, Donat, et al., 2018; Wang & Zhou, 2024). Beyond long-term warming trends, recent studies have highlighted the importance of ~~large-scale climate variability~~large-scale climate modes in enhancing MHW characteristics globally through atmospheric and oceanic teleconnections (Holbrook et al., 2019; Wang & Zhou, 2024). For example, El Niño-Southern Oscillation (ENSO) influences MHWs over the tropical Pacific and Indian Oceans (Hamdeno et al., 2024; Liu et al., 2022; Mohamed et al., 2022; Oliver, Perkins-Kirkpatrick, et al., 2018; Vivekanandan et al., 2008). During El Niño phases, the significant increases in sea surface temperature (SST) lead to prolonged MHWs in the eastern tropical Pacific (Podesta & Glynn, 2001). Similarly, the North Atlantic Oscillation (NAO) primarily affects the tropical and North Atlantic MHWs (Gröger et al., 2024; Holbrook et al., 2019; Mohamed et al., 2023; Scannell et al., 2016). Although current forecast systems show skills in predicting the occurrence of MHWs in the El Niño region (de Boisséson & Balmaseda, 2024), with prediction accuracy significantly improving during El Niño events (Jacox et al., 2022), the forecast accuracy remains poor in the Northeastern Atlantic Ocean influenced by NAO, particularly in the North Sea (de Boisséson & Balmaseda, 2024; McAdam et al., 2023). This limitation warrants further investigations into the mechanisms driving MHWs at the relevant spatio-temporal scales.

The North Sea is a shelf sea located on the passive continental margin of northwest Europe, connecting the Baltic Sea to the Atlantic. The SST and MHW patterns in this region are influenced by large-scale North Atlantic ~~climate variabilities~~climate modes, including NAO, the Atlantic Multidecadal Variability (AMV) and East Atlantic Pattern (EAP) (Mohamed et al., 2023; Mohamed et al., 2025; Scannell et al., 2016; van der Molen & Pätsch, 2022). Distinct seasonal differences of MHW mechanisms and climate ~~variability~~ modes responses in the North Sea have been documented (Gröger et al., 2024; Mohamed et al., 2023). Summer and winter exhibit contrasting patterns: during summer, MHWs are more frequent with higher intensity but shorter duration, while winter shows fewer events with lower intensity but longer duration. The NAO and EAP represent the two dominant modes of atmospheric circulation variability over the Euro-Atlantic region (Thornton et al., 2023), while AMV refers to large-scale multidecadal fluctuations in Atlantic SST (Kerr, 2000). These ~~climate variabilities~~climate modes regulate westerly winds in the North Atlantic, affecting warm Atlantic inflow into the southern North Sea (van der Molen & Pätsch, 2022). Existing studies show that MHW frequency in the southern North Sea increases during the positive phase of AMV or EAP, while positive NAO primarily intensifies winter MHW occurrence (Mohamed et al., 2023; Scannell et al., 2016). The southern North Sea, characterized by shallow depths (Fig. 1a), experiences low-frequency, high-intensity, and long-duration MHWs. In contrast, the northern North Sea, which features larger water depth, exhibits more frequent and intense, but shorter MHWs (Chen & Staneva, 2024). However, the underlying dynamic mechanisms remain poorly understood (Mohamed et al., 2023).

Moreover, historical studies have indicated that ~~climate variabilities~~climate modes in the Atlantic Ocean are interconnected (Börgel et al., 2020; Delworth & Zeng, 2016; Delworth et al., 2017; Sun et al., 2015). For example, the AMV alters the zonal position of NAO centers of action (Börgel et al., 2020), while the NAO-Atlantic Meridional Overturning Circulation interaction shapes the AMV (Delworth & Zeng, 2016; Delworth et al., 2017; Sun et al., 2015). These Atlantic climate variations also connect with Pacific Ocean patterns (Oshika et al., 2015). The AMV modulates the impact of Arctic Oscillation on ~~ENSO and~~ tropical climate variability (Chen et al., 2025; Xue et al., 2025). Conversely, ENSO-induced dipolar convection anomalies exert an influence on NAO and EAP (Brönnimann, 2007; Hou et al., 2023; Jiménez-Esteve & Domeisen, 2018; Scaife et al., 2024; Wicker et al., 2024). Existing literature (Gröger et al., 2024; Hamdeno et al., 2024; Liu et al., 2022; Mohamed et al., 2023) has focused primarily on the effects of individual ~~climate variabilities~~climate modes on MHWs, leaving their synergistic influence largely unexplored.

In this study, we address ~~aim to fill~~ the knowledge gap in understanding synergistic impacts of ~~climate variabilities~~climate modes on MHWs in shelf seas. We focus on the greater North Sea region, which is projected to warm as fast as global levels (Hobday & Pecl, 2014) but exhibits large climate variability caused by interactions between the Arctic and subtropical zones (Quante & Colijn, 2016). This makes it an ideal regional example for understanding how ~~climate variabilities~~climate modes synergistically influence MHWs in complex shelf sea settings. Specifically, this study aims to (1) identify coherent spatial domains in the North Sea based on the seasonal patterns of interannual marine heatwave cumulative intensity (MHWCI) variability, (2) quantify how the frequency, intensity, and duration of MHWs differ between these domains during their seasonally dominant periods, and (3) examine the associated atmospheric and oceanic processes that modulate the observed regional contrasts. A correlation-based k-means clustering approach is used to characterize MHWCI variability, followed by an examination of the associated large-scale climate variability, air-sea heat fluxes, and oceanic heat transport.

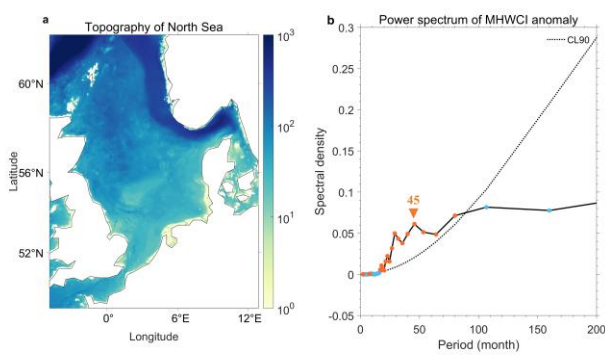

带格式的: 居中

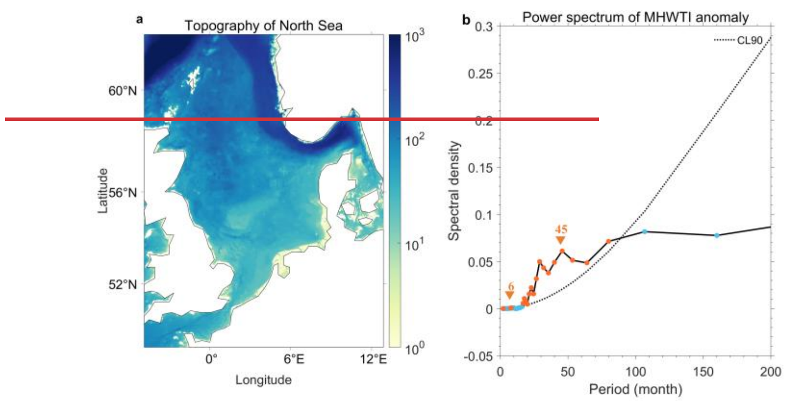

Figure 1. (a) The research domain of the North Sea. The bathymetry (m) is shown on a logarithmic scale. (b) Power spectrum analysis of 12-month running-mean marine heatwave cumulative intensity (MHWCI) anomalies in the North Sea derived from OSTIA. Orange dots indicate periods exceeding the 90% confidence level (black dashed line), while blue dots represent periods below this threshold. The 90% confidence level is calculated using a χ^2 test against a red-noise (AR(1)) background spectrum based on the lag-1 autocorrelation.

设置了格式: 字体: (中文) 宋体, (中文) 简体中文(中国大

带格式的: 两端对齐, 缩进: 首行缩进: 0 厘米

2 Data and Methods

2.1 Data

2.1.1 SST and MHW Identification

设置了格式: 字体: (中文) 宋体, (中文) 简体中文(中国大

Our analysis of MHWs in the North Sea (Fig. 2a) is based on high-resolution SST data (0.05°×0.05°, daily) obtained from the Copernicus Marine Environment Monitoring Service (CMEMS). This product is generated by the Operational Sea Surface Temperature and Sea Ice Analysis ~~This dataset integrates multiple satellite measurements and in-situ observations by the Operational Sea Surface Temperature and Sea Ice Analysis~~ (OSTIA) ~~(Good et al., 2020; Worsfold et al., 2024),~~ , which integrates multiple satellite observations and in situ measurements, and covers the period 1982-2021~~covering the period 1982-2021~~. An independent observation-based SST dataset from the FerryBox system (Macovei et al., 2021)~~Another observation-based SST data used for validation is from the FerryBox (V. Macovei et al., 2021; V. A. Macovei et al., 2021)~~, developed by Helmholtz-Zentrum Hereon, is used for validation purposes (Fig. S1)~~which was developed by Helmholtz-Zentrum Hereon (Fig. A1)~~.

MHWs, which are defined as individual thermal events during which their associated temperature is larger than the 90th percentile threshold for at least 5 days (Hobday et al., 2016), are detected by using the MATLAB Marine Heatwaves (M_MHW) toolbox (Zhao & Marin, 2019). The climatological mean and percentile-based threshold used to detect MHW events are computed over the period 1982-2021, which corresponds to the full temporal coverage of the SST dataset used in this study. To ensure internal consistency across all analyses, a unified climatological baseline and detrending strategy is applied throughout this study. All anomalies are computed relative to the same reference period, and long-term trends are removed before analyses that focus on variability and climate-mode relationships.

The long-term warming trend was subtracted to better estimate the effects of climate modes (Liu et al., 2022). To isolate variability relative to the long-term warming background, SST was detrended before MHW detection. The detrending was performed by identifying a linear trend estimated from the global-mean SST time series over 1982-

2021 and subtracting this common trend from the SST time series at each grid point. This procedure reduces the influence of externally forced warming on the identification of marine heatwaves and subsequent analyses.

Characteristics of MHWs, including frequency, duration, mean intensity, and cumulative intensity, were derived following event detection. Among these metrics, cumulative intensity integrates the effects of event duration and mean intensity and provides an effective measure of the overall impact of MHWs (Marin et al., 2021). In this study, the cumulative intensity was summed to derive the monthly MHWCI, representing the combined impact of all MHW events occurring within a given month (Gröger et al., 2024; Mohamed et al., 2023). Specifically, the cumulative intensity of all MHW events whose onset date falls within a given month was summed to form the monthly MHWCI, while months without any MHW events were assigned a value of zero. This results in a continuous monthly MHWCI time series, which was subsequently expressed as anomalies relative to its long-term mean to characterize interannual variability

2.1.2 Atmospheric and oceanic reanalysis data

Atmospheric conditions were characterized using the ERA5 reanalysis dataset (Hersbach et al., 2020) produced by ~~from~~ the European Centre for Medium-Range Weather Forecasts (ECMWF~~), ~~). ERA5 provides~~which provides daily~~ monthly variables at a spatial at resolution of~~at~~ 0.25°×0.25°~~ resolution from 1970 to present~~. The variables used in this study include 10-m wind components, 500-hPa geopotential height, precipitation, and surface heat fluxes.~~These variables include 10-m wind components, 500-hPa geopotential height, precipitation, and heat flux.~~ Although ERA5 is available from 1940 onward, only data from 1982-2021 were used in this study to ensure consistency with the satellite-based SST record used for marine heatwave detection.

Oceanic conditions were analyzed using monthly ~~For oceanic variables, including potential temperature and current velocity, we used monthly~~ data from the ECMWF Ocean Reanalysis System 5 (ORAS5) (Zuo et al., 2019), which provides global ocean reanalysis data at a horizontal resolution of 0.25°. Variables of interest include potential temperature and ocean current velocity, which were used to examine subsurface thermal structure and oceanic heat transport associated with MHW variability. Our analysis focuses on seasonal to interannual variability, for which monthly-mean fields are commonly used in existing studies (Liu et al., 2022; Mohamed et al., 2023).~~.~~

~~2.2 Cumulative intensity of MHW~~

~~MHWs, which are categorized as a thermal event when their associated temperature is larger than the 90th percentile threshold for at least 5 days (Hobday et al., 2016), are detected by using the MATLAB Marine Heatwaves (M_MHW) toolbox (Zhao & Marin, 2019). The long-term warming trend was subtracted to better estimate the effects of climate variability (Liu et al., 2022). The MHW metrics include frequency, duration, mean intensity, and cumulative intensity. The potential impact of individual events on marine ecosystems is best represented by their cumulative intensity, combining the effect of duration and average intensity (Marin et al., 2021). In this study, the cumulative intensity was summed to derive the monthly cumulative intensity (MHWCI), which represents the intensity over the duration of MHW events occurring within one month (Gröger et al., 2024; Mohamed et al., 2023).~~

2.1.3 Climate modes

The influence of large-scale climate modes is investigated using indices of the NAO, the EAP, and the AMV, which are known to modulate atmospheric circulation over the North Atlantic and adjacent shelf seas. The NAO and EAP indices are obtained from the National Oceanic and Atmospheric Administration (NOAA) Climate Prediction Center and are derived from the first and second modes of a rotated empirical orthogonal function (EOF) analysis of monthly mean 500-hPa geopotential height anomalies over the North Atlantic.

带格式的: 缩进: 首行缩进: 1.27 厘米

设置了格式: 字体: (中文) Times New Roman, 检查拼写和语法

带格式的: Heading-Main, 左

设置了格式: 字体: (中文) 宋体, (中文) 简体中文(中国大陆)

带格式的: 缩进: 首行缩进: 0 厘米

带格式的: Text, 两端对齐

The AMV index is derived from basin-averaged SST anomalies over the North Atlantic. To isolate internal multidecadal variability, the AMV index is calculated by removing the global-mean SST anomaly from the North Atlantic mean SST anomaly (Trenberth & Shea, 2006). Positive and negative phases of each climate mode are defined using a fixed threshold at zero, with values greater (less) than zero indicating positive (negative) phases. Seasonal indices are computed by averaging the corresponding monthly values over the relevant seasons.

Previous studies have shown that positive phases of the AMV and EAP are associated with increased annual MHW cumulative intensity in the North Sea, whereas positive NAO phases primarily enhance wintertime MHW occurrence in the southern North Sea (Mohamed et al., 2023; Mohamed et al., 2025).

2.~~3~~ 2 K-means Clustering Analysis

Distinct regional patterns of MHWCI variability in the North Sea were identified using a correlation-based K-means clustering approach (Jain, 2010; Lloyd, 1982). Unlike conventional K-means clustering, which minimizes Euclidean distance, ~~Unlike the conventional K-means that minimizes the Euclidean distance,~~ the correlation-based version groups spatial grid points according to the similarity in the shape of their normalized feature vectors, thereby emphasizing pattern similarity rather than absolute amplitude. Such correlation-based K-means clustering has been successfully applied in gene expression data analyses (Logananthara j et al., 2006) and brain connectivity dynamics (Allen et al., 2014), where spatial units are grouped based on similarities in their temporal or spatial variability structures to identify coherent regions. ~~to identify regions with coherent temporal or spatial variability patterns.~~

Given the pronounced seasonal variability of MHW in this region, this approach classifies grid points ~~areas~~ according to their seasonally resolved interannual variability characteristics~~seasonal patterns of MHWCI interannual variability~~, rather than applying the clustering separately to individual seasons. ~~,~~ Specifically, a K-means clustering is performed using seasonal variability information derived from the full monthly record, thereby revealing spatially coherent regions with distinct seasonal responses to large-scale climate forcing.~~reflecting different regional responses to large-scale climate forcing,~~

设置了格式: 字体: (中文) Times New Roman

For each grid point, MHWCI anomalies were computed for each season by subtracting the long-term seasonal climatology. The four seasons are defined as winter (December of the previous year and January-February of the current year, DJF), spring (March-May, MAM), summer (June-August, JJA), and autumn (September-November, SON), which correspond to well-established physical regimes in the North Sea (Chen & Staneva, 2024; Mohamed et al., 2023), including wintertime deep mixing and weak stratification, and summertime strong stratification with shallow mixed layers. ~~The four seasons were defined as winter (December of the previous year and January–February of the current year, named as DJF), spring (from March to May, named as MAM), summer (from June to August, named as JJA), and autumn (from September to November, named as SON).~~ The interannual variability during each season was quantified as the standard deviation of anomalies across the 40 years, yielding a four-component feature vector per grid point, with each component representing DJF, MAM, JJA, and SON variability. To reduce the influence of extreme values and ensure equal weighting among the four seasonal components, a logarithmic transformation followed by standardization was applied to the feature vectors. The dissimilarity between two grid points (Eq. 1) was defined as the correlation distance between their feature vectors:

$$D(x_i, x_j) = 1 - r(x_i, x_j), \qquad (1)$$

where $r(x_i, x_j)$ is the Pearson correlation coefficient between the seasonal variability patterns of MHWCI, emphasizing the similarity in their seasonal variability structures. The total within-cluster dissimilarity was computed as the sum of squared correlation distances (WCSS), which decreases as the number of clusters K increases. The number of clusters K was determined using the Elbow Method, where the reduction in WCSS begins to level off (Syakur et al., 2018). In this study, K=2 was selected as the optimal number of clusters (Figure ~~B1~~A1). Further validation of clustering robustness is provided in Appendix ~~B~~A. This number results in two well-separated and spatially coherent regions in the North Sea, broadly corresponding to the southern and northern subregions, indicating distinct temporal variability characteristics of MHWCI.

Based on the assessment, grid points were partitioned into two clusters by grouping them with similar seasonal patterns. Each cluster is characterized by its dominant season, defined as the season with the highest mean standardized variability, and the relative contributions of all four seasons. This approach identifies regions where MHWCI variability exhibits specific seasonal dependence, thereby revealing distinct spatial patterns that may be linked to different large-scale climate variations.

2.3 Quantification of upper-ocean stratification

To characterize the upper-ocean stratification associated with MHWs, mixed layer depth (MLD) is diagnosed following a density-based criterion. Specifically, MLD is defined as the depth at which the potential density first exceeds the potential density at 10 m by 0.03 kg m⁻³ (England et al., 2025), which has been shown to be suitable for shallow and seasonally stratified shelf seas. Vertical stratification and dynamical stability are further quantified using the gradient Richardson number, *Ri*, defined as:

$$Ri = \frac{N^2}{S^2}, \quad (3)$$

where *N* is the buoyancy frequency,

$$N = \left(-\frac{g}{\rho}\frac{\partial \rho}{\partial z}\right)^{1/2}, \quad (4)$$

and *S* is the vertical shear

$$S = \left[\left(\frac{\partial u}{\partial z}\right)^2 + \left(\frac{\partial v}{\partial z}\right)^2\right]^{1/2} \quad (5).$$

Here, *g* denotes gravitational acceleration, *ρ* is seawater density, and *u* and *v* are the zonal and meridional velocity components, respectively. All variables are derived from the ORAS5 reanalysis and are computed over the same temporal intervals as the temperature fields to ensure consistency among stratification and heat budget diagnostics.

(Mohamed et al., 2023; Mohamed et al., 2025; Trenberth & Shea, 2006)

2.~~4~~ 4 Heat budget analysis

The physical processes driving MHWCI variations in the subregions identified by the K-means clustering were quantitatively examined through an upper-ocean heat budget analysis. After linearizing the variables, the perturbation equation of upper ocean heat anomalies (Eq. ~~2~~3) can be described as (Liu et al., 2014; Tan et al., 2016):

$$\frac{\partial \mathrm{T}'_m}{\partial \mathrm{t}} = \frac{Q'_{net}}{\rho C_p \mathrm{h}_m} - \left(\vec{\bar{\mathrm{u}}}_g \cdot \vec{\nabla}\mathrm{T}'_m + \vec{u}'_g \cdot \vec{\nabla}\overline{\mathrm{T}}_m\right) - \left(\vec{\bar{\mathrm{u}}}_e \cdot \vec{\nabla}\mathrm{T}'_m + \vec{u}'_e \cdot \vec{\nabla}\overline{\mathrm{T}}_m\right) - \left(\overline{\mathrm{w}}_e \frac{(\mathrm{T}_m - \mathrm{T}_d)'}{\mathrm{h}_m} - \mathrm{w}'_e \frac{\overline{(\mathrm{T}_m - \mathrm{T}_d)}}{\mathrm{h}_m}\right) + RES, \quad (~~2~~6)$$

where the overbar and prime denote the monthly mean and anomaly, respectively. The left-hand side represents the sea surface temperature anomaly tendency. We calculated this tendency as the temperature difference between February and ~~November~~ December for winter and between August and ~~May~~ June for summer, respectively. The right-hand side comprises four main terms, namely the net heat flux, geostrophic heat advection, Ekman heat advection, and entrainment heat flux~~-~~, respectively. The last term denotes the residual term (*RES*), which includes nonlinear heat advection and diffusion, etc. These terms are averaged over the respective seasonal periods. Q'_{net} refers to the sea surface net heat flux anomaly, comprising the net shortwave and longwave radiative components, as well as the net latent and sensible heat fluxes. Positive values of Q'_{net} indicate ocean gaining heat from the atmosphere. ρ is the seawater density (1025 ~~kg~~ kg/m^{-3}), C_p is the specific heat capacity (3890 J kg^{-1} K^{-1}), and h_m is the ~~mixed layer depth (~~MLD.~~), (England et al., 2025)~~ ~~defined as the depth where temperature decreases by 0.5°C from the surface~~

设置了格式: 字体: (中文) Times New Roman, 10 磅, 字体颜色: 文字 1
设置了格式: 字体: (中文) Times New Roman, 10 磅, 字体颜色: 文字 1
带格式的: Heading-Main, 左
设置了格式: 字体: 倾斜
设置了格式: 10 磅, 字体颜色: 文字 1, 不检查拼写或语法
设置了格式: 10 磅, 字体颜色: 文字 1, 不检查拼写或语法
设置了格式: 10 磅, 字体颜色: 文字 1, 不检查拼写或语法
设置了格式: 10 磅, 字体颜色: 文字 1, 不检查拼写或语法
设置了格式: 10 磅, 字体颜色: 文字 1, 不检查拼写或语法
设置了格式: 10 磅, 字体颜色: 文字 1, 不检查拼写或语法
带格式的: 居中
设置了格式: 字体: 倾斜
带格式的: 左
带格式的: 居中
设置了格式: 字体: 倾斜
带格式的: 居中
设置了格式: 字体: 倾斜
设置了格式: 字体: 倾斜
设置了格式: 字体: 倾斜
设置了格式: 字体: 倾斜
设置了格式: 10 磅, 字体颜色: 文字 1, 不检查拼写或语法
设置了格式: 字体: 10 磅, 加粗, 检查拼写和语法, 字距调整14 磅
设置了格式: 字体: (中文) 宋体, (中文) 简体中文(中国大陆)
设置了格式: 字体: (中文) 宋体, (中文) 简体中文(中国大陆)
设置了格式: 字体: (中文) Times New Roman

~~value(Monterey & Levitus, 1997) (Monterey & Levitus, 1997).~~ ORAS5 provides ocean variables on 75 vertical levels, with vertical spacing increasing from approximately 1 m near the surface, allowing a physically consistent estimation of MLD and mixed-layer heat budget terms at seasonal to interannual timescales. The horizontal circulation in the surface layer can be divided into the Ekman current component $\vec{u}_e$ and the geostrophic current component $\vec{u}_g$. w_e is the Ekman pumping (entrainment) velocity, with positive values indicating Ekman upwelling, pumping or divergence and negative values for Ekman downwelling or convergence, respectively. T_m is the mixed-layer temperature, and is set to SST in this study for simplicity. T_d is the temperature below the base of the mixed layer. This heat tendency equation (Eq. 6) follows the standard formulation commonly used in upper-ocean heat budget studies. All terms are computed using monthly mean fields.

设置了格式: 字体: (中文) Times New Roman

2.~~5~~ 5 Horizontal wave activity flux

Large-scale atmospheric teleconnections influence the formation and persistence of MHWs by modulating atmospheric circulation and surface heat fluxes. The Pacific-Atlantic teleconnection is closely linked to Rossby wave propagation (Hou et al., 2023). The propagation of these teleconnection signals was diagnosed using the wave activity flux (WAF, Eq. ~~3~~7), which quantifies the direction and intensity of stationary Rossby wave energy propagation (Takaya & Nakamura, 2001). Hence, the horizontal WAF (unit: m² s⁻²) was calculated as follows:

$$WAF = \frac{p\cos\varphi}{2|U|}\begin{bmatrix} \frac{U}{a^2\cos^2\varphi}\left[\left(\frac{\partial\psi'}{\partial\lambda}\right)^2-\psi'\frac{\partial^2\psi'}{\partial\lambda^2}\right]+\frac{V}{a^2\cos\phi}\left(\frac{\partial\psi'}{\partial\lambda}\frac{\partial\psi'}{\partial\varphi}-\psi'\frac{\partial^2\psi'}{\partial\lambda\partial\varphi}\right) \\ \frac{U}{a^2\cos\varphi}\left(\frac{\partial\psi'}{\partial\lambda}\frac{\partial\psi'}{\partial\varphi}-\psi'\frac{\partial^2\psi'}{\partial\lambda\partial\varphi}\right)+\frac{V}{a^2}\left[\left(\frac{\partial\psi'}{\partial\varphi}\right)^2-\psi'\frac{\partial^2\psi'}{\partial\varphi^2}\right] \end{bmatrix}, \quad (\text{~~3~~}7)$$

where p is the pressure normalized to 1000 hPa, φ is the latitude, λ is the longitude, a is the radius of the Earth, $\psi(=\varphi/f)$ is the geostrophic stream function, φ (m) is the geopotential height, f is the Coriolis parameter and ψ' is the perturbed stream function. $|U|$, U and V represent the averaged wind speed, zonal, and meridional wind velocity, respectively.

3 Results

3.1 Seasonal-to-decadal variability of MHWs

Power spectrum analysis of the detrended monthly MHWCI (Fig. 1b), constructed as a continuous time series by summing the cumulative intensity of all MHW events occurring within each month (and set to zero when no events occur), shows that ~~the original signal is dominated by seasonal variability (not shown)~~, after removing the dominant seasonal pattern, substantial variability remains at interannual timescales~~whereas the spectrum in Fig. 1b, based on a 12-month running mean, highlights variability at interannual timescales.~~~~Power spectrum analysis of the detrended monthly MHWCI reveals two distinct temporal patterns, namely a seasonal variation and an interannual variation, both significant at the 90% confidence level (Fig. 1b).~~ Several spectral peaks exceed the 90% confidence level, suggesting that MHWCI variability in the North Sea is organized on multi-year timescales. This provides a basis for exploring whether such variability exhibits coherent spatial and seasonal structures across the region.

Based on the seasonal patterns of interannual MHWCI ~~interannual~~ variability, the correlation-based K-means clustering identifies ~~analysis identified~~ two spatially coherent ~~distinct~~ subregions (named as Cluster 1 and 2, respectively) in the North Sea (Fig. 2a). Cluster 1 mainly covers the central and southern parts of the North Sea, while Cluster 2 includes the deeper northern ~~part~~region. The two clusters are geographically contiguous and broadly aligned with the contrast between the shallow southern shelf and the deeper northern basin.

Seasonal differences between the two clusters were quantified by calculating the relative contribution of each season, expressed as the percentage of its spatially averaged interannual variability intensity (VI) relative to all four seasons within each cluster. Positive values of VI indicate seasons that contribute more strongly to the total variability of that cluster, while negative values indicate weaker contributions.

In Cluster 1, variability is dominated byCluster 1 is characterized by pronounced variability in winter (VI = 0.66) and autumn (VI = 0.41), with substantially weaker variability in summer (VI = -0.28) and spring (VI = 0.07) (Fig. 2b). Cluster 2, by contrast, shows its strongest variability in summer (VI = 0.57) and moderate variability in spring (VI = 0.24), while variability in autumn (VI = -0.08) and winter (VI = -0.30) is relatively weak.Cluster 1 shows the highest variability in winter (VI = 0.66) and autumn (VI = 0.41), but lower variability in summer (VI = -0.28) and spring (VI = 0.07) (Fig. 2b). In contrast, Cluster 2 exhibits strong variability in summer (VI = 0.57) and moderate variability in spring (VI = 0.24), while autumn (VI = -0.08) and winter (VI = -0.30) are characterized by low variability. These results indicate a clear seasonal asymmetry between the central-southern and northern North Sea, implying that seasons with the most active MHW-related variability differ between the two regionsimplying that MHW-related variability is most active in different seasons across the two regions.

highlight that the two regions exhibit pronounced differences in the season during which interannual MHWCI variability is strongest. In the central-southern North Sea (Cluster 1), variability is dominated by winter, whereas in the northern deeper region (Cluster 2) it is primarily expressed in summer. These seasonal contrasts are derived from the relative contributions of each season to the standardized interannual variability of MHWCI and therefore reflect when MHW-related variability is most active in each region. Based on this diagnosis, the subsequent analyses focus on winter MHWCI for Cluster 1 and summer MHWCI for Cluster 2 in order to examine large-scale climate influences during the season of maximum variability for each region. The relationship between regional differences and large-scale climate modes was examined using the time series of domain-average MHWCI extracted for each cluster. Consistent with the identified seasonal dominance, the winter series was analyzed for Cluster 1 and the summer series for Cluster 2.

While the clustering analysis identifies when MHWCI variability is most pronounced in each region, it does not indicate which MHW characteristics primarily contribute to the enhanced cumulative intensity. To address this, composite analysis of MHW frequency, intensity, and duration anomalies werewas examined during positive phases of the cluster-specific MHWCI time series (Fig. 3). In Cluster 1, enhanced winter MHWCI is associated with concurrent increases in MHW frequency, intensity, and duration (Fig. 3a-c), indicating that winter MHWs in the central and southern North Sea become more frequent, persistent, and intense. In contrast, enhanced summer MHWCI in Cluster 2 is mainly associated with increases in MHW frequency and duration, while mean intensity shows a slight reduction (Fig. 3d-f). This suggests that summer MHWs in the northern North Sea tend to be more persistent but less intense.

Based on the seasonal dominance and the contributing MHW characteristics identified above, the temporal evolution of the cluster-mean MHWCI and its relationship with large-scale climate indices is examined (Fig. 2c-d). In Cluster 1 (mainly central and southern North Sea), the winter-averaged MHWCI exhibits pronounced interannual variability, with enhanced values tending to coincide with positive phases of EAP (r = 0.64, 95% confidence interval). In addition, negative phases of the negative NAO in the preceding October frequently precede winters with elevated MHWCIphases in late autumn (October, blue shading in Fig. 2c) are frequently followed by a positive winter EAP, which is significantly correlated with enhanced winter MHWCI (r = 0.64, 95% confidence interval).

For In Cluster 2 (mainly northern North Sea), the summer-averaged MHWCI displays pronounced decadal modulation (Fig. 2d)demonstrates distinct responses depending on the phase of the AMV. During the negative AMV phase (1982-1994, blue shading in Fig. 2d), MHWCI exhibits relatively weak intensity. In contrast, during the positive AMV phase (1994-2013, red shading in Fig. 2d), MHWCI shows notable enhancement, with its interannual variability strongly correlated with both ENSO and the Interdecadal Pacific Oscillation (IPO) (r = 0.69 and 0.70, respectively).

带格式的: 缩进: 首行缩进: 0 厘米
设置了格式: 字体: 10 磅, 倾斜
设置了格式: 字体: 倾斜
设置了格式: 字体: 10 磅, 倾斜
设置了格式: 字体: 10 磅, 倾斜
设置了格式: 字体: 倾斜
设置了格式: 字体: 10 磅, 倾斜
设置了格式: 字体: 10 磅, 倾斜
设置了格式: 字体: 倾斜
设置了格式: 字体: 10 磅, 倾斜
设置了格式: 字体: 10 磅, 倾斜
设置了格式: 字体: 倾斜
带格式的: Abstract, 缩进: 首行缩进: 1.27 厘米

However, this teleconnection substantially weakens after 2013 (Fig. S2), with correlations becoming statistically insignificant ($p > 0.1$), indicating a substantial reduction in Pacific influence on North Sea MHWs.

These results demonstrate that MHWCI variability in the North Sea is organized into two spatially distinct regions with contrasting seasonal dominance, MHW characteristics, and temporal ~~behavior~~behaviour. Based on these differences, subsequent analyses focus on winter MHWs in Cluster 1 and summer MHWs in Cluster 2 to investigate the associated atmospheric and oceanic processes. ~~indicate that the dominant climate drivers of MHWCI variability differ across regions and timescales: Cluster 1 is primarily shaped by late autumn NAO in combination with winter EAP, while Cluster 2 is modulated by summer Pacific telecommunications that vary with AMV phase. This spatial and temporal diversity suggests that MHWCI in the southern and northern parts of the North Sea is driven by distinct atmospheric circulation patterns and associated oceanic processes.~~

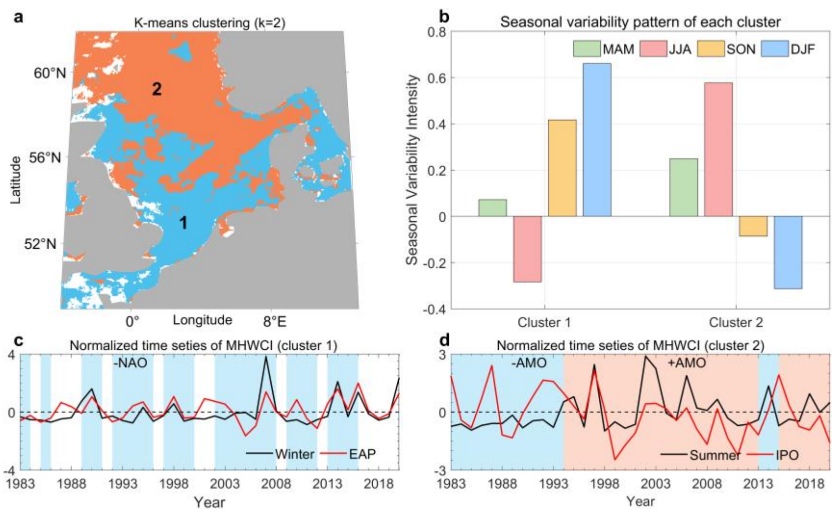

Figure 2. K-means clustering of marine heatwave cumulative intensity (MHWCI) in the North Sea and associated climate ~~variability~~modes. (a) Spatial distribution of two clusters based on the seasonal patterns of interannual MHWCI variability. (b) Seasonal variability of each cluster. Positive values indicate seasons with stronger contributions to interannual variability, while negative values indicate weaker contributions. (c) Z-score normalized~~Normalized~~ time series of domain-averaged MHWCI for Cluster 1 during winter (black) and the East Atlantic Pattern (EAP, red); blue shading denotes negative NAO phases in October of the preceding year. (d) Z-score normalized~~Normalized~~ time series of domain-averaged MHWCI for Cluster 2 during summer (black) and Interdecadal Pacific Oscillation (IPO) index (red); blue and red shading indicate negative and positive phases of Atlantic Multidecadal Variability (AMV), respectively. All time series in (c) and (d) are standardized using z-score normalization and are therefore dimensionless. The blue bar from 2013-2015 indicates the Atlantic "cold blob" event.

~~Composite analysis of MHW frequency, intensity, and duration anomalies during positive MHWCI periods highlights the underlying mechanisms (Fig. 3). In Cluster 1, the winter MHWCI increase is driven jointly by higher frequency, intensity, and duration (Fig. 3a-c). In Cluster 2, summer MHWCI enhancement is characterized by increased frequency and duration but decreased intensity (Fig. 3d-f), indicating that summer conditions promote persistent but less intense MHWs in the northern North Sea.~~

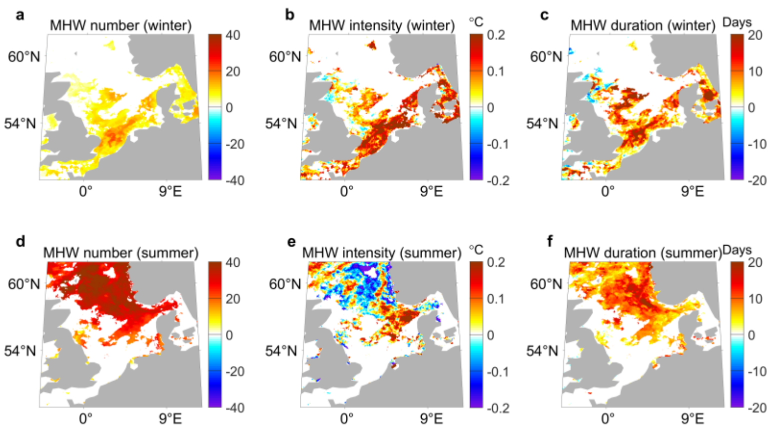

Figure 3. Composite anomalies of MHW characteristics during positive phases of the cluster-specific time series in winter (a-c) and summer (d-f). (a, d) MHW number, (b, e) MHW intensity (°C), and (c, f) MHW duration (days).

3.2 Cluster 1: Winter Mechanisms in the Central and Southern North Sea

The atmospheric and oceanic conditions associated with enhanced winter MHWCI in Cluster 1 were examined using composite anomalies during periods when the standardized cluster-mean MHWCI exceeds +1 standard deviation~~The influence of climate variability modes on winter MHWCI in Cluster 1 through atmospheric processes was examined by compositing atmospheric variables during periods of enhanced MHWCI , defined as times when the standardized cluster-specific time series exceeds +1 standard deviation~~ (black line in Fig. 2c)~~(positive phase of black line in Fig. 2c)~~. The analysis focuses on large-scale atmospheric circulation, surface forcing, and oceanic circulation and heat transport during the months from October of the preceding year to January of the MHW winter.

Figure 4 shows the composite anomalies of ~~including~~ 500-hPa geopotential ~~height~~ ~~, wind stress,~~and WAF (Eq. 7) from October of the preceding year to January of the MHW winter~~, and heat flux anomalies~~. The anomalous WAF flux is shown only when its magnitude is larger than 0.1 m^2/s^2 (Hou et al., 2023).

~~In~~In October, during enhanced MHWCI periods, the geopotential ~~height~~ anomalies, defined relative to the long-term monthly climatology, exhibit pronounced negative anomalies over the subpolar North Atlantic, with positive anomalies observed over the subtropical and polar regions (Fig. 4a). ~~–~~This atmospheric configuration corresponds to a negative NAO phase, characterized by a weakened Azores High and intensified Icelandic Low. ~~The resulting cyclonic wind anomalies decrease SST over the central North Atlantic (Fig. 5a).~~Additionally, the WAF vectors indicate relatively weak wave activity over the eastern Atlantic.

In November, the system enters a transition phase. The negative geopotential anomalies over the subpolar Atlantic intensify and extend eastward, while positive anomalies expand toward northern Europe (Fig. 4b). During this period, an eastward-propagating Rossby wave train becomes apparent, with WAF vectors indicating energy propagation from the North American sector toward the eastern North Atlantic. ~~SST cooling extends northward (Fig. 5b) under the influence of cyclonic circulation anomalies. Meanwhile, negative geopotential height anomalies over the subpolar and polar Atlantic intensify, while positive anomalies extend northeastward. An eastward-propagating Rossby wave train develops, with WAF originating from the North American coast and propagating toward western Europe (Fig. 4b).~~

设置了格式: 上标

设置了格式: 上标

带格式的: 缩进: 首行缩进: 1.27 厘米

By December, the wave train includes both eastward and westward-propagating components across the North Atlantic. This WAF configuration generates strong convergence over the subpolar region, significantly reinforcing the negative geopotential ~~height~~ anomalies there. Consequently, the atmospheric pattern transitions to a positive EAP phase. The geopotential ~~height~~ field displays a distinct tripole structure, reflecting intensified Azores High and Icelandic Low systems, accompanied by a strengthened high-pressure system over western Europe (Fig. 4c). ~~The associated cyclonic winds maintain reduced SST in the subpolar region (Fig. 5c).~~ This configuration persists into January (Fig. 4d~~)), sustaining southwesterly wind anomalies over the northeastern North Atlantic (Fig. 5d)~~.

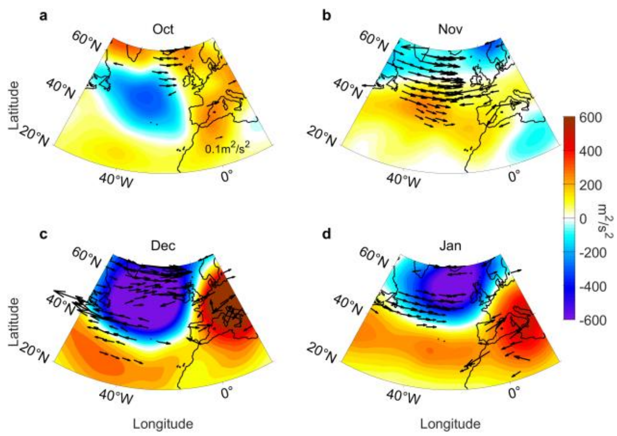

Figure 4. Composite anomalies of 500-hPa geopotential ~~height~~ (shading, m^2/s^2) and horizontal wave activity flux (WAF, vector, m^2/s^2) from October of the preceding year to January of the following year, based on winters with positive values in the cluster-specific time series. The anomalous WAF flux is shown only when its magnitude is larger than 0.1 m^2/s^2.

The sea surface temperature (SST) and wind stress anomalies from October to January are illustrated in Fig. 5. In October, anomalous cyclonic wind stress is observed over the central North Atlantic, accompanied by negative SST anomalies in the same region (Fig. 5a). In November, the region of SST cooling expands northward and eastward, following the intensification of cyclonic wind anomalies over the subpolar Atlantic (Fig. 5b). By December and January, strengthened southwesterly wind anomalies are evident over the northeastern North Atlantic and the North Sea region (Fig. 5c-d). During these months, SST anomalies over the southern North Sea become positive, in contrast to the persistent negative SST anomalies over the subpolar Atlantic. These patterns indicate a clear spatial contrast in surface thermal ~~pattern~~patterns between the open North Atlantic and the shelf region during winters with enhanced MHWCI in Cluster 1.

带格式的: 缩进: 首行缩进: 1.27 厘米

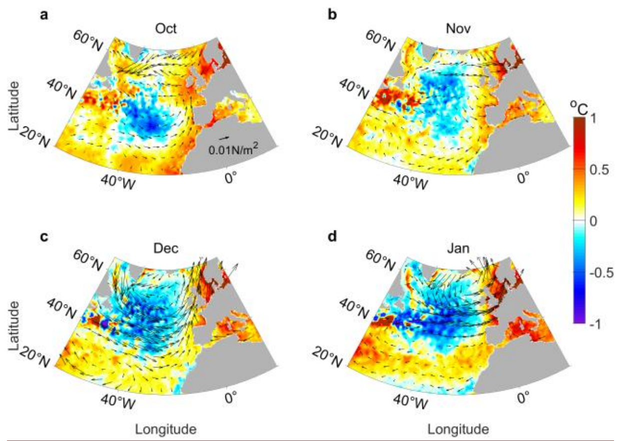

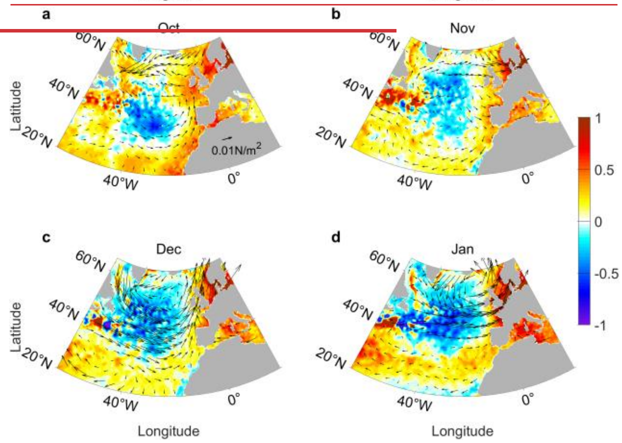

Figure 5. Composite anomalies of sea surface temperature (shading, ºC) and wind stress (vectors, N/m^2) from October of the preceding year to January of the following year, based on winters with positive values in the cluster-specific time series.

Figure 6 presents composite anomalies of the net surface heat flux and its individual components averaged over the Cluster 1 region during winters with enhanced MHWCI. The net surface heat flux anomaly is negative, indicating a net loss of heat from the ocean to the atmosphere. Among the individual components, the sensible heat flux exhibits the largest negative anomalies, while latent heat flux anomalies are weaker in magnitude. The radiative components show comparatively small anomalies, with shortwave and longwave radiation partially compensating each other. The dominance of the sensible heat flux anomaly is consistent with the strengthened near-surface winds observed during these winters. The surface heat flux anomalies indicate that atmospheric forcing acts to cool the ocean surface over the Cluster 1 region during periods of enhanced MHWCI.

These southwesterly winds enhance sensible heat loss from the ocean to the atmosphere, which serves as the primary contributor to negative net heat flux anomalies when averaged over the Cluster 1 region (blue bar in Fig. 6). By contrast, these southwesterly wind anomalies modify the ocean current convergence over the southern North Sea (Fig. 7b), enhancing SST. To further investigate the ocean response, circulation anomalies were composited during periods of enhanced MHWCI. The strengthened subtropical westerlies since late autumn enhance the transport of warm North Atlantic waters (Fig. 7a), increasing northward heat transport into the North Sea through the English Channel (Mohamed et al., 2023; van der Molen & Pätsch, 2022), and raising SST in the southern North Sea. After entering the North Sea, anomalous southwesterly winds drive this warm water northward, enhancing both meridional and zonal overturning circulations (MOC and ZOC) in the central North Sea (Fig. 7d, e). These strengthen oceanic downwelling and heat content (Fig. 7c), further offsetting the cooling from reduced net heat flux, illustrating the combined atmospheric and oceanic mechanisms driving winter MHWCI in Cluster 1. Additionally, the warm water inflow reduces cold outflow from the Baltic Sea.

To further characterize the local upper-ocean state during winter MHW conditions, composite anomalies of MLD and stratification-related variables were examined. In winter, the southern and central North Sea is predominantly well mixed due to strong wind forcing and shallow bathymetry, as reflected by weak climatological stratification with low N^2 and Ri. Consistent with this background state, composite MLD anomalies during positive MHWCI winters are generally weak, with noticeable signals confined to very shallow shelf regions. Over most of the southern and central North Sea, anomalies in N^2 and Ri remain small, indicating limited modification of the winter mixed regime.

带格式的: 缩进: 首行缩进: 0 厘米

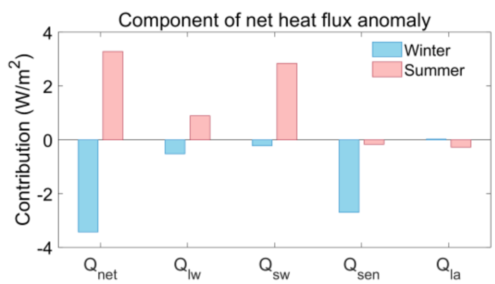

Figure 6. Composite anomalies of net heat flux and its components (W/m^2) in the North Sea during winters (blue bars) and summers (red bars) with positive values in the cluster-specific time series. Components include shortwave (Q_{sw}) and longwave (Q_{lw}) radiation, as well as the net latent (Q_{la}) and sensible (Q_{sen}) heat flux anomalies. Positive values indicate ocean heat gain from the atmosphere, while negative values indicate heat loss.

Figure 7 shows composite anomalies of oceanic circulation and stratification-related variables during enhanced MHWCI winters. The surface current anomalies (Fig. 7a) reveal enhanced northward and eastward flow at the southern entrance of the North Sea, indicating increased inflow from the adjacent North Atlantic. Within the southern and central North Sea, the current anomalies exhibit convergence, as reflected by the spatial arrangement of the velocity vectors. Additionally, the warm water inflow reduces cold outflow from the Baltic Sea.

In winter, the Cluster 1 region is predominantly well mixed due to strong wind forcing and shallow bathymetry, as reflected by weak climatological stratification (Fig. S4a) with low *Ri* (Fig. S3). Consistent with this background state, composite MLD anomalies (Fig. 7b) are negligible across most of the Cluster 1 region, with negative anomalies confined to very shallow shelf regions.

设置了格式: 字体: 倾斜

设置了格式: 非突出显示

The Richardson number anomalies displayed in Fig. 7c exhibit a similar spatial structure. While *Ri* anomalies are weak or near zero over the well-mixed central basin, pronounced negative anomalies appear in the same shallow shelf regions where MLD shoaling is observed. This spatial correspondence indicates that changes in stratification and velocity shear are spatially collocated over shallow shelf areas during enhanced MHWCI winters.

设置了格式: 字体: 倾斜

These localized structural changes occur together with coherent atmospheric and oceanic anomalies. Enhanced Atlantic inflow provides a positive contribution to the mixed-layer heat budget, while strengthened southwesterly winds are associated with increased surface heat loss. Additionally, shoaling of the MLD reduces the effective heat capacity of the upper ocean, allowing advected heat to produce a stronger temperature response. Meanwhile, reduced *Ri* indicates enhanced shear relative to stratification, which modulates vertical mixing without promoting deep redistribution of heat. Consequently, heat transported by horizontal advection can be preferentially retained in the near-surface layer, favoring the development and persistence of winter MHWs despite concurrent surface heat loss.

To further assess the dynamical response associated with these coupled structural and heat transport anomalies, the corresponding overturning circulation anomalies are investigated~~examined below~~. Figure 7d presents composite anomalies of the meridional overturning circulation (MOC) during enhanced MHWCI winters. The ~~overturning circulation~~MOC is strengthened, with increased northward and downward transport in the southern and central North Sea, respectively. These overturning features align with regions of enhanced Atlantic inflow and current convergence. The enhanced downward transport in the central North Sea occurs within a water column that is already well mixed during winter. As a result, the intensified overturning circulation does not produce a discernible mixed-layer deepening, consistent with the absent MLD and *Ri* anomalies observed in the central basin. Instead, the enhanced overturning facilitates the redistribution and retention of advected heat within the water column, contributing to elevated winter temperatures and enhanced MHWCI in the central North Sea.

设置了格式: 字体: 倾斜

设置了格式: 字体: 倾斜

带格式的: 缩进: 首行缩进: 1.27 厘米

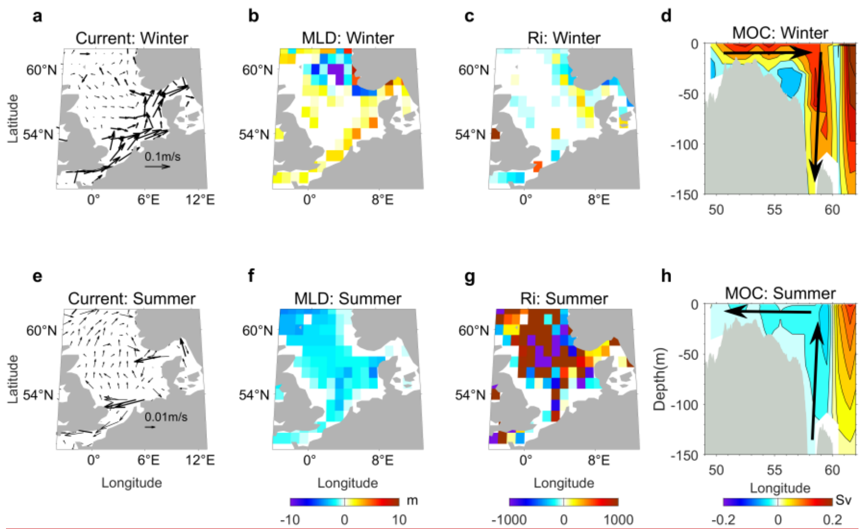
a
Current: Winter
b
MLD: Winter
c
Ri: Winter
d
MOC: Winter
e
Current: Summer
f
MLD: Summer
g
Ri: Summer
h
MOC: Summer
60°N
54°N
0°
6°E
12°E
8°E
Latitude
Longitude
Depth(m)
0.1m/s
0.01m/s
m
-10
0
10
-1000
1000
Sv
-0.2
0.2
-50
-100
-150
50
55
60

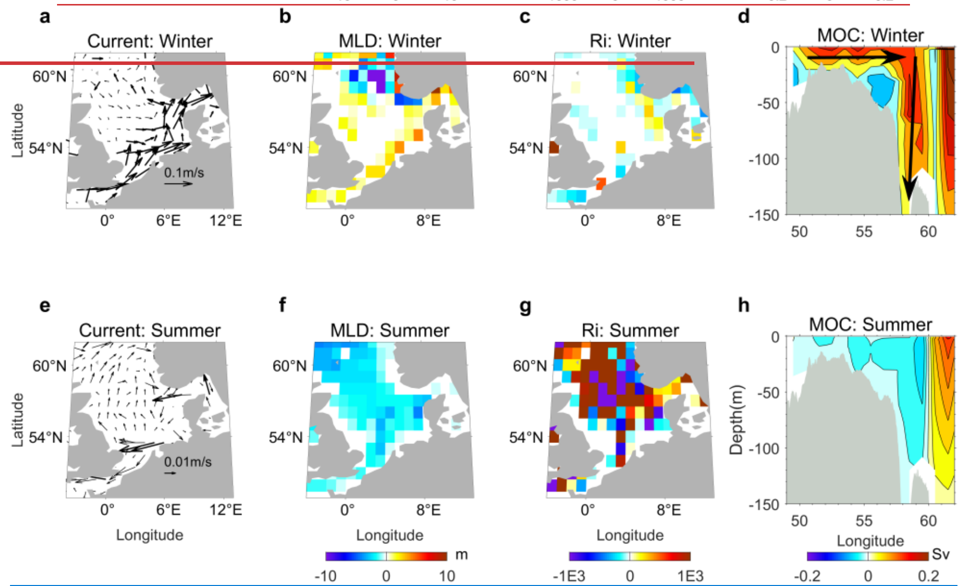
a
Current: Winter
b
MLD: Winter
c
Ri: Winter
d
MOC: Winter
e
Current: Summer
f
MLD: Summer
g
Ri: Summer
h
MOC: Summer
60°N
54°N
0°
6°E
12°E
8°E
Latitude
Longitude
Depth(m)
0.1m/s
0.01m/s
m
-10
0
10
-1E3
1E3
Sv
-0.2
0.2
-50
-100
-150
50
55
60

带格式的: 居中

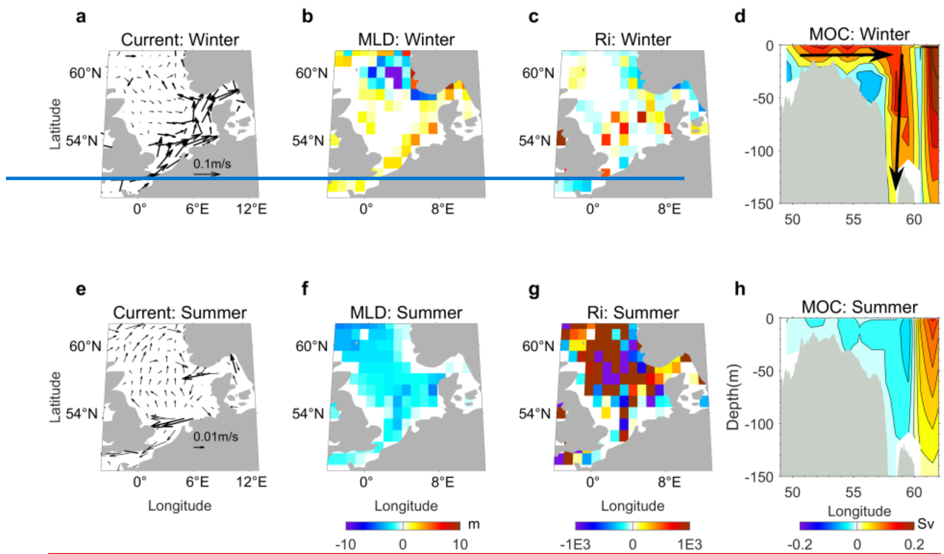

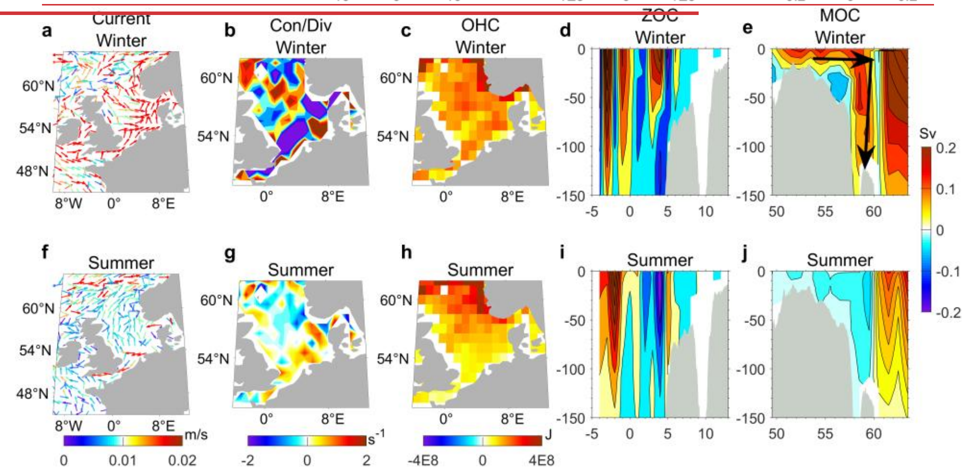

Figure 7. Composite anomalies of oceanic variables during positive phases of the cluster-specific time series in winter (a-~~e~~d) and summer (~~f~~e-~~j~~h). (a), (~~f~~e) ~~Geostrophic o~~Oceanic current (vectors, m/s), (b), (~~g~~f) ~~convergence and divergence of advection~~mixed layer depth (MLD, ~~s^{-1}~~m), (c), (~~h~~g) Richardson number (*Ri*)~~ocean heat content (J)~~, (d), (~~i~~h) ~~zonal overturning circulations (ZOC, Sv), (e), (j)~~ meridional overturning circulations (MOC, Sv). The MOC is domain-integrated overturning circulations, obtained by integrating the velocity field over the entire zonal and meridional extent of the study domain, respectively. Negative stream function values correspond to clockwise circulation, while positive values indicate counterclockwise circulation. Black arrow-headed lines in (d) and (h) indicate the direction of the overturning circulation. ~~The black arrow-headed lines represent the direction of flow.~~

设置了格式: 字体: 倾斜

The relative contributions of different processes to the upper-ocean temperature tendency during winter are quantified using a mixed-layer heat budget analysis (Eq. 6, Fig. 8). The total temperature tendency is positive, indicating net warming over the winter season in Cluster 1. Among the individual terms, geostrophic heat advection provides the largest positive contribution to the temperature tendency, while the contribution from surface heat flux is negative. Ekman advection and entrainment terms are comparatively small, and the residual term contributes weakly. The relative magnitudes of the heat budget terms indicate that horizontal ocean heat transport supplies a substantial positive contribution to wintertime warming, partially offsetting the cooling effect associated with surface heat loss.

The upper-ocean heat budget for Cluster 1 was examined to evaluate the relative contributions of different mechanisms. Result shows that winter warming in the southern-central North Sea is primarily driven by geostrophic heat advection (Fig. 8), consistent with the enhanced Atlantic inflow through the English Channel (Fig. 7a). These results indicate that winter MHW frequency, intensity and duration in Cluster 1 are largely influenced by the North Atlantic climate variabilitiesclimate modes through both atmospheric and oceanic pathways via enhanced westerly winds and strengthened Atlantic inflow.

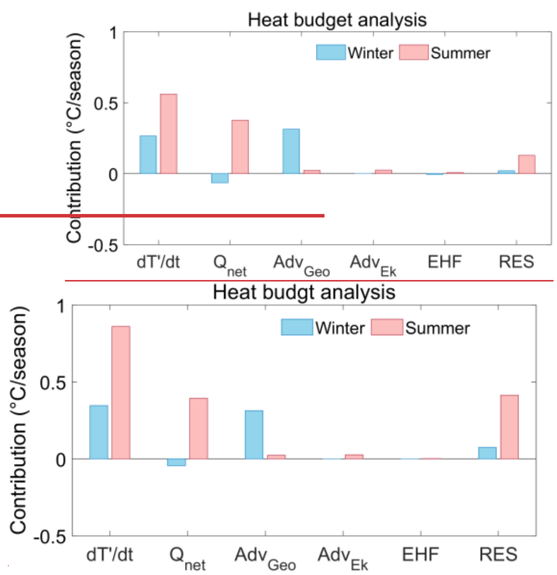

Figure 8. Quantitative contribution (˚C/season) of atmospheric and oceanic processes to the upper ocean temperature anomaly tendency for two clusters identified by the K-means algorithm. The atmospheric and oceanic variables are shown as composite patterns during positive phases of the cluster-specific time series in winter (blue) and summer (red). The temperature tendency (*dT'/dt*) represents the difference in the sea surface temperature anomaly between February and DecemberNovember for winter and between August and JuneMay for summer, respectively. Contributions from the net heat flux anomaly (Q_{net}), geostrophic heat advection (Adv_{Geo}), Ekman heat advection (Adv_{Ek}), entrainment heat flux (*EHF*), and residual term (*RES*), averaged over the same periods, are also shown.

3.3 Cluster 2: Summer Mechanisms in the Northern North Sea

We examine summer variability in Cluster 2 -by comparing the period of strong positive AMV (1994-2012) with the post-2013 period and the negative AMV phase. The phase-dependent atmospheric and oceanic conditions are examined using regression patterns of atmospheric and oceanic variables onto the IPO index, with Fig. 9 presenting the associated large-scale circulation and WAF anomalies, and Fig. 10 showing the corresponding surface wind stress, SST, cloud cover, and precipitation responses. This analysis highlights that IPO-related atmospheric responses are substantially stronger during the positive AMV period than during the later or negative phases.

During the strong positive AMV phases (1994-2012), the regression patterns over the North Pacific exhibitsexhibit a clear geopotential dipole, with positive anomalies over the subpolar Pacific and negative anomalies over the subtropical Pacific. The contrast between these anomaly centers is accompanied by strengthened zonal wind anomalies between these regions (Lin et al., 2023), indicating an intensified large-scale atmospheric response over the Pacific. Consequently, the WAF vectors form an eastward propagation pathway from the Pacific across North America toward the North Atlantic, with substantially larger magnitudes than during other phases (Fig. 9a). This pattern documents an efficient transmission of atmospheric perturbations from the Pacific into the Atlantic during the positive AMV period.

Consistent with the strengthened large-scale circulation anomalies, regression patterns of SST (Fig. 10a) show warming along the west coast of North America and a broader, resembling the canonical positive IPO structure (Fig. 10a). Over the Caribbean Sea (black box in Fig. 10b), northeasterly wind anomalies coincide with reduced precipitation and negative SST anomalies, indicating suppressed convection in this region. We identified the synergetic impact of AMV and Pacific teleconnectionstelecommunications on the summer MHWCI in the North Sea. Comparison of atmospheric variable regression patterns onto the IPO index reveals stronger atmospheric responses in the North Pacific Ocean during strong positive AMV phases (1994-2012). The possible underlying mechanism can be explained through a sequence of atmospheric interactions. First, positive AMV induces anomalous ascent over the North Atlantic and anomalous descent over the North Pacific, which forms a dipole pattern of geopotential height with positive anomalies over the subpolar Pacific and negative anomalies over the subtropical Pacific (Fig. 9a). These interactions induce easterly wind anomalies between these regions (Lin et al., 2023). As a result, an anomalous cyclonic wind pattern emerges over the subtropical Pacific, strengthening ENSO-associated westerly winds and enhancing SST in the tropical Pacific Ocean (Hou et al., 2023). The associated warming along the North American west coast is consistent with the positive IPO phase (Fig. 10a).

The enhanced tropical and subtropical Pacific responses are transmitted across ocean basins through Rossby wave energy propagation. The WAF vectors clearly indicate the propagation of Rossby wave energy from the Pacific toward the North Atlantic, particularly under the positive AMV phase (Fig. 9a). This intensified wave propagation facilitates more efficient transmission of atmospheric perturbations from the Pacific, across North America, and into the Atlantic region. As part of this teleconnection pattern, northeasterly wind anomalies develop over the Caribbean Sea, reducing precipitation and SST in this region (Fig. 10b). Theis suppressed convection modifies the regional Rossby wave source, exhibit an eastward propagation pathway from North Atlantic to the North Sea (Fig. 9a). The corresponding enhanced geopotential reduced cloud cover over the northern North Sea (black box in Fig. 10c). Additionally, contributing to the maintenance of the anticyclonic pattern over the subtropical western North Atlantic. over the northeastern Atlantic and the northwestern North Sea, Tthe associated southeasterly wind anomalies over the northwestern North Sea (Fig. 10a) suppress Atlantic moisture transport, , further maintaining the decreased cloud cover.

The reduced cloud cover over the northern North Sea is accompanied by enhanced downward shortwave radiation, as reflected by the positive shortwave component of the net surface heat flux (Fig. 5). The summer heat budget further confirms the dominance of surface forcing during this period: surface heat flux and the residual (RES) term provide the primary positive contributions, while horizontal and vertical advection remain comparatively weak (Fig. 8). This surface-flux-dominated heat budget differs fundamentally from winter conditions in Cluster 1, where geostrophic advection plays a leading role.

reducing cloud cover the over the northern North Sea (Fig. 10c), which increases downward shortwave radiation (red bars in Fig. 5), further contributing to enhanced downward net surface heat flux.

The effect of surface radiative forcing in summer is closely linked to the upper-ocean structure in Cluster 2. During summer, the climatological MLD is extremelyquite shallow (Fig. S4b). Composite anomalies further show a basin-wide shoaling of the MLD in Cluster 2 (Fig. 7f), implying a further shoaling of the near-surface layer during enhanced MHWCI summerthat the near-surface layer becomes even thinner. Fig 7g also shows predominantly positive *Ri* anomalies over the same region, indicating enhanced stratification stability dynamical stability and a

设置了格式: 字体: 倾斜

reduced susceptibility to shear-driven instabilities. The spatial co-location of MLD shoaling and increased Ri suggests that buoyancy-driven stratification strengthens sufficiently to offset any increase in velocity shear, resulting in a more stably stratified upper ocean during these summers. Together, these changes imply that radiative and surface heat flux anomalies are confined to a thin surface layer, allowing relatively short-lived atmospheric forcing anomalies to produce a pronounced near-surface thermal response.

In addition to surface forcing, the regression patterns indicate a dynamical response in the regional circulation. The easterly wind anomalies counteract the climatological southwesterlies, leading to weakened surface winds over the northern North Sea. These wind anomalies are accompanied by negative MOC anomalies (Fig. 7i), indicating an anomalous anticlockwise overturning circulation with enhanced upwelling over the northern North Sea. When combined with the summer upper-ocean structure (shallow MLD and increased *Ri*), this circulation configuration provides a consistent explanation for the observed MHW characteristics in Cluster 2: a shallow, stably stratified surface layer increases the sensitivity of SST to radiative anomalies, favoring more frequent and longer-lasting warm events, whereas the upwelling-related cooling tendency limits the buildup of extreme surface warming, consistent with reduced MHW intensity.Heat budget analysis further confirms that in summer the MHW response in Cluster 2 is dominated predominated by the surface heat flux and the RES term, whereas horizontal and vertical advection are comparatively weak (Fig. 8). During summer, the MLD is extremely shallow in Cluster 2 (13.2 m on average, decreasing to 12.5 m during positive phases), in contrast to much deeper winter MLD in Cluster 1 (88.9 m on average, and 84.9 m for positive phases). This shallow, strongly stratified surface layer enables short-lived radiative anomalies to trigger and prolong MHWs, while limited oceanic heat advection constrains subsurface heat storage, consistent with the absence of notable intensification in MHW intensity.

设置了格式: 字体: 倾斜

The easterly wind anomalies counter the prevailing climatological southwesterly winds. The resulting wind weakening generates cyclonic circulation anomalies in the northern North Sea (Fig. 7f), causing anomalous convergence of horizontal flows (Fig. 7g). These anomalous eastward inflows entering the North Sea produce positive ZOC anomalies (Fig. 7i), increasing ocean heat content (Fig. 7h). Although these circulation changes contribute locally to heat accumulation, their contribution to the overall heat budget is minor, indicating that geostrophic advection exerts only a limited influence on MHWCI variability in the Cluster 2 region (Fig. 8).

In contrast to winter conditions, summer stratification in the northern North Sea is much more pronounced. The climatological mixed layer is shallow, accompanied by elevated N^2 and Ri values. During positive MHWCI summers, composite anomalies show a basin-wide shoaling of the MLD and a concurrent increase in N^2, indicating enhanced vertical stratification. Richardson number anomalies exhibit large magnitudes and pronounced spatial heterogeneity, particularly in the northern North Sea, reflecting strongly reduced vertical mixing during MHW conditions.

After 2013, previous studies have documented an abrupt cooling in the subpolar North Atlantic the cold anomaly developed in the Atlantic Ocean (Mooney, 2015), often referred to as the development of the "cold anomaly" or "cold blob," which coincides with a weakening of the AMV signal during the early 2010s (Frajka-Williams et al., 2017; Josey & Sinha, 2022; Moat et al., 2020)coinciding with a weakening AMV signal (Frajka-Williams et al., 2017). During this period, the tropical and subtropical Pacific exhibit markedly diminished atmospheric responses (Fig. 10d-f). Tropical Pacific SST anomalies weaken substantially compared to 1994-2012, accompanied by the reductions in precipitation. Moreover, the geopotential height anomalies in the North Pacific weaken significantly (Fig. 9b), and the dipole circulation pattern between the subpolar and subtropical Pacific substantially weakens. WAF analysis reveals a marked disruption of Rossby wave energy propagation from the Pacific to the Atlantic (Fig. 9b).

This Pacific-Atlantic teleconnection weakens even further during the negative AMV phase. The geopotential height dipole in the Pacific is much less pronounced (Fig. 9c), further diminishing the dipole circulation and reducing zonal wind anomalies between these regions. The SST anomaly distribution remains inconsistent with the IPO spatial pattern, with the North American coastal warming signature nearly absent (Fig. 10g). Correspondingly, the westerly wind anomalies over the tropical Pacific are substantially more suppressed. This also suppresses the Rossby wave source, leading to a marked reduction of eastward Rossby wave energy flux into the Atlantic region (Fig. 9c). The diminished atmospheric response produces minimal impacts on North Atlantic circulation and limited modification of the North Sea (Fig. 10 h-i).

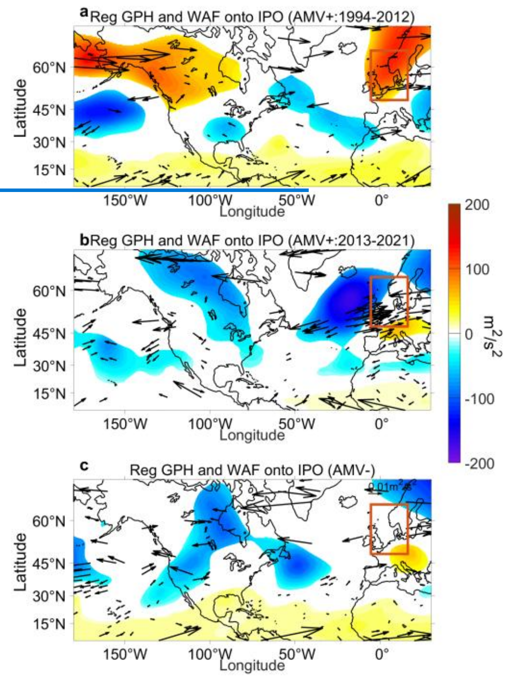

带格式的: 居中

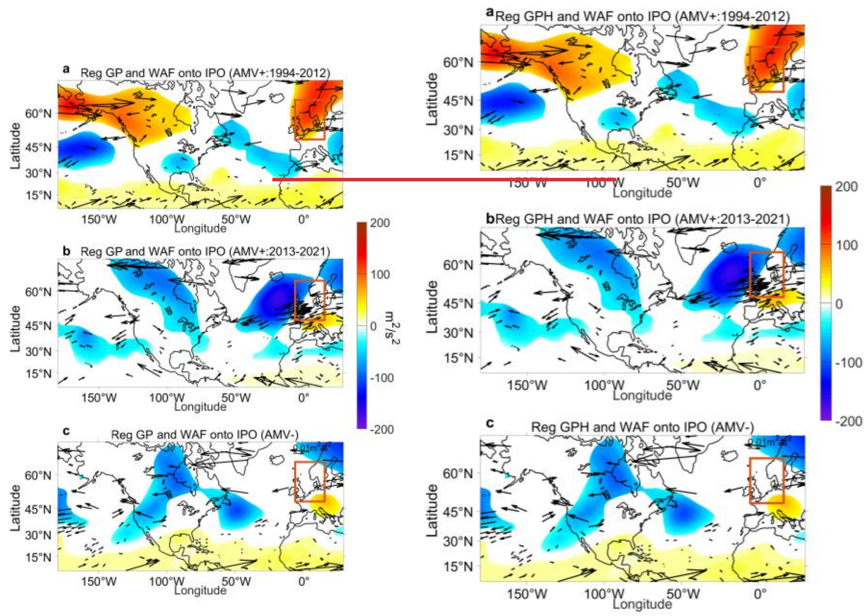

Figure 9. Summer Composite patterns of 500-hPa geopotential ~~height~~ anomalies (shading, m^2/s^2) and horizontal WAF (vector, m^2/s^2) during (a) positive AMV phase (1994-2012), (b) positive AMV phase (2013-2021), and (c) negative AMV phase. All fields are regressed onto the IPO index. Only significant anomalies at the 90% confidence level are shown. The orange box indicates the North Sea region. ~~(图片标题的 GPH 要修改)~~

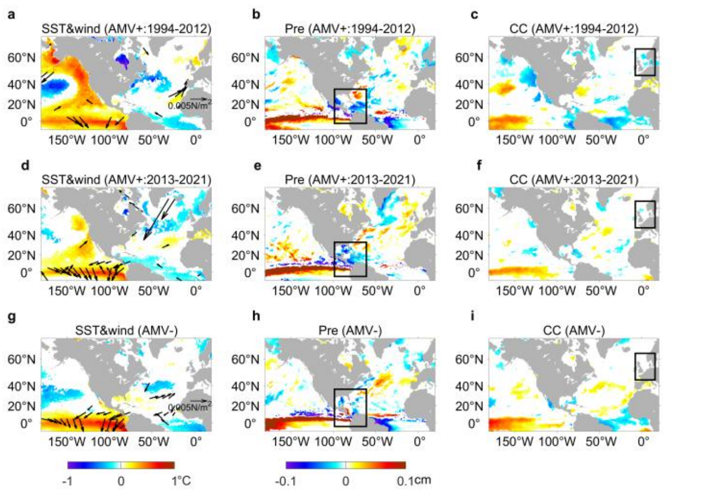

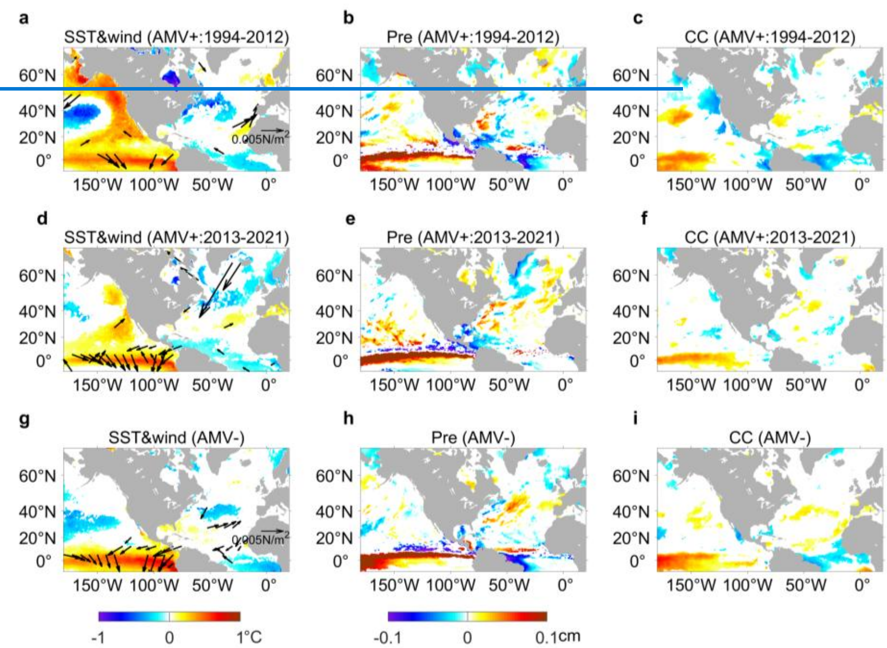

Figure 10. Summer atmospheric patterns regressed to the IPO index during different AMV phases. Composite anomalies during positive AMV phase (1994-2012) (a-c), positive AMV phase (2013-2021) (d-f), and negative AMV phase (g-i): (a), (d), (g) wind stress (vectors, N/m^2) and sea surface temperature (SST, shading, °C), (b), (e), (h) precipitation (cm), and (c), (f), (i) cloud cover. Only significant anomalies at the 90% confidence level are shown. The black boxes in (b), (e), and (h) indicate the Caribbean Sea. The black boxes in (c), (f), and (i) indicate the North Sea region.

4 Discussion

4.1 Contrasting climate influences in MHWs across the North Sea

Our analysis of observed SST data demonstrates how multiple ~~climate variabilities~~climate modes interact to influence MHWs at a regional scale through seasonally distinct mechanisms. Different from previous studies that mainly applied clustering analysis to group heatwaves based on common characteristics (Artana et al., 2024; Chauhan et al., 2023), location (Hansen, 2024), and underlying dynamic drivers (Vogt et al., 2022), this study employed a correlation-based k-means clustering approach to further explore their spatial and temporal coherence. Our analysis identified two distinct regions in the North Sea, a southern shallow region and a northern deep region, each dominated by different climate variations and seasonal dynamics. Similar north-south spatial contrasts in MHW-induced stratification associated with water depth have also been reported in the North Sea (Chen et al., 2022).

In the central-southern shallow North Sea (Cluster 1), enhanced MHWCI is closely linked to positive winter EAP conditions, typically following a negative late-autumn NAO. Previous studies have shown that MHW frequency in the southern North Sea increases during positive phases of either NAO or EAP (Mohamed et al., 2023). Similar NAO-related influences have also been reported in the adjacent Baltic Sea (Gröger et al., 2024). Our results refine this understanding by identifying the positive winter EAP as the primary driver, enhancing not only the frequency but also the intensity and duration.

Recent research also indicates that ~~AMO~~AMV plays a more important role than the NAO in influencing the frequency of summer MHWs in the southern North Sea (Mohamed et al., 2023). However, its role in the northern North Sea has received little attention. Our results show that in Cluster 2, representing the deeper northern North Sea, the enhanced MHW frequency and duration in summer is linked to the synergistic influence of the AMV and Pacific ~~climate variabilities~~climate modes. These teleconnections propagated from the Pacific to the North Sea through Rossby wave energy propagation, which is consistent with studies emphasizing the role of Pacific teleconnections in shaping the North Atlantic atmospheric pattern (Hou et al., 2023).

To exclude the influence of long-term warming, the SST data were linearly detrended before computing the MHW metrics. Even after detrending, Cluster 2 exhibits increasing frequency and duration accompanied by a slight decrease in intensity during positive MHWCI periods. This result is consistent with basin-wide observations from 1993 to 2022, which show a declining trend of MHW intensity but increasing frequency and duration (Chen & Staneva, 2024). Such a change is attributed to large-scale atmospheric circulation changes and regional oceanic processes rather than global warming. The reduction in intensity has been proposed to be related to the weakening of the North Atlantic Jet Stream and more frequent atmospheric blocking events (Woollings et al., 2018), which promote stagnant atmospheric conditions and persistent but less intense warm anomalies over the North Sea, while freshwater-salt exchange, stratification changes, and Baltic Sea inflow also modulate regional SST responses (Mathis & Pohlmann, 2014). As an additional possible mechanism, the interannual-decadal variability linked to the AMV and Pacific teleconnections could modulate the summer North Atlantic atmospheric pattern, which then changes MHW intensity in the northern North Sea.

4.2 Global implications and future perspectives

Current MHW forecast systems exhibit the highest skill in the El Niño region, the Caribbean, the wider tropics, the north-eastern extra-tropical Pacific, and southwest of the extra-tropical basins. However, the skill is much lower in the ~~western Mediterranean and rather poor in the~~ North Sea, whatever the forecast range (de Boisséson & Balmaseda, 2024; Jacox et al., 2022). This is likely due to the impact of unresolved atmospheric variability, limited representation of teleconnections and climate modes (Ardilouze et al., 2017; Patterson et al., 2022). Since climate indices serve as important forecasting factors influencing these events (Jacox et al., 2022; Mi et al., 2025), incorporating synergistic climate interactions into forecasting frameworks could enhance predictive skill for MHWs.

Similar teleconnection mechanisms have been documented in other shelf seas and marginal seas, including the Baltic Sea (Gröger et al., 2024) and South China Sea (Deng et al., 2022). For instance, the Indian Ocean Basin-Wide index has been identified as a key predictor of long-term MHWs occurrence in the South China Sea (Mi et al., 2025), while including ENSO-related variability in the tropical Pacific may extend the duration of ~~skillful~~ skilful forecasts of atmospheric patterns over the North Atlantic (Shackelford et al., 2025). Our results reveal clear regional and seasonal contrasts in how large-scale climate variations influence MHW variability across the North Sea. These contrasts highlight that MHW predictability in shelf seas depends on the timing, location, and combined effects of multiple climate drivers rather than their individual ~~strength~~ strengths alone. Incorporating these spatially and seasonally varying relationships into forecast systems would allow models to improve the ability to forecast when and where MHWs are most likely to occur.

5 Conclusions

By applying a correlation-based k-means clustering approach, this study revealed coherent spatial and temporal patterns of MHWCI variability in the North Sea and their connections to large-scale climate variations. The results show that multiple interacting ~~climate variabilities~~climate modes jointly drive MHWCI variability on the northeastern Atlantic shelf, emphasizing the need to consider combined effects rather than individual forcing mechanisms.

The relative importance and mechanisms of these large-scale drivers vary regionally and seasonally~~:~~. In winter, MHWCI variability in the southern North Sea is primarily regulated by~~the~~ EAP, ~~exerts stronger control in the southern North Sea during winter,~~ acting through two complementary pathways: an atmospheric pathway associated with strengthened southwesterly winds, and an oceanic pathway characterized by increased Atlantic inflow and strengthened MOC. Under a wintertime well-mixed pattern, enhanced ocean heat transport contributes to elevated water-column temperatures, favoring the development of winter MHWs (Fig. 11a). ~~through two pathways, namely an atmospheric bridge via enhanced southwesterly winds and an oceanic pathway through strengthened Atlantic inflow (Fig. 11a).~~

In contrast, summer MHWCI variability in the northern North Sea is dominated by the combined influence of the ~~the~~ AMV and Pacific-related teleconnections ~~dominate in the northern region during summer~~. During positive AMV phases, strengthened IPO-like atmospheric responses in the Pacific enhance Pacific–Atlantic teleconnections via Rossby wave energy propagation~~the dipole geopotential height pattern along the North American west coast, reinforces IPO-like structures and strengthens Pacific-Atlantic teleconnections~~. These teleconnections modulate cloud cover and surface radiative forcing over the North Sea, leading to a surface-flux-dominated heat budget in summer. The shallow mixed layer and enhanced stratification, reflected by reduced MLD and increased *Ri*, increase the sensitivity of surface temperature to atmospheric forcing and suppress vertical redistribution of heat. Concurrently, changes in regional overturning circulation, including enhanced upwelling in the northern North Sea, limit the accumulation of extreme surface warming. As a result, summer MHWs in this region are characterized by increased frequency and duration but reduced intensity ~~These teleconnections, propagated from the tropical and subtropical Pacific to the North Atlantic through Rossby wave energy propagation, ultimately influence cloud cover over the North Sea and alter sea-air heat fluxes~~ (Fig. 11b). When the AMV transitions to neutral or negative phases after 2013,~~When the AMV is in transitions to neutral or negative phases,~~ the weakening of IPO-like patterns reduces Pacific-Atlantic coupling, thereby diminishing their influence on the region. Together, these regionally and seasonally distinct mechanisms provide a clear physical basis for how ~~large-scale climate variability~~large-scale climate modes modulate~~s~~ MHWs in shelf seas.

设置了格式: 字体: 倾斜

These findings have practical implications for enhancing process-based prediction and for understanding how MHW characteristics may respond to future changes in ~~large-scale climate variability~~large-scale climate modes. Future research should test whether similar interaction patterns occur in other shelf seas, evaluate the potential of climate indices to improve MHW prediction skill, and investigate how the underlying mechanisms may change under future climate conditions.

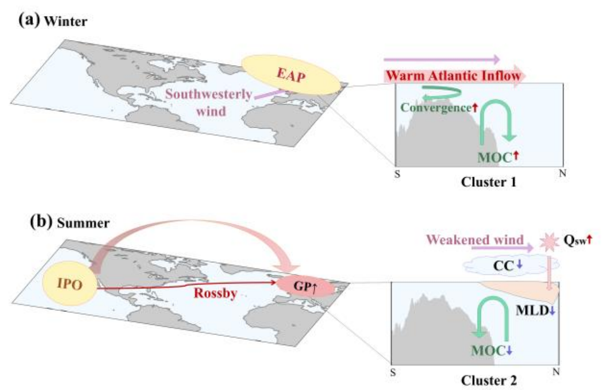

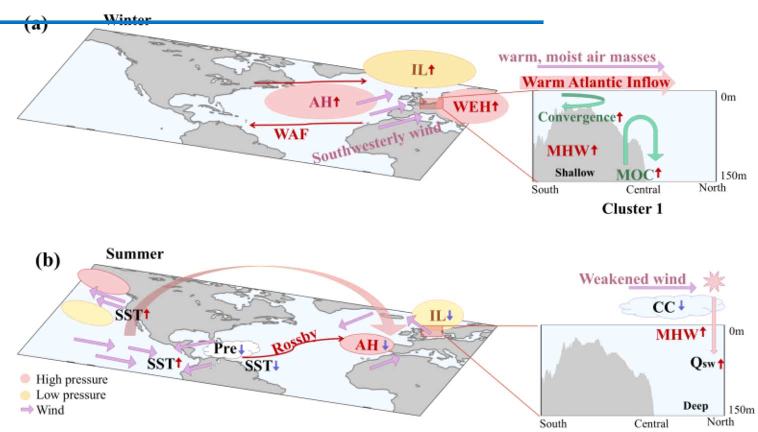

Figure 11. Schematic illustration of two distinct cluster patterns showing the synergistic impacts of climate ~~variability~~ modes on MHWCI in the Northwestern European shelf. (a) ~~Winter~~ The winter pattern characterized by a combined negative NAO phase in late autumn and a positive EAP phase in winter. (b) ~~Summer~~ The summer pattern characterized by simultaneous positive phases of AMV~~, PDO,~~ and ~~El Niño~~IPO. Purple arrows indicate wind anomalies. ~~Red and yellow circles denote high and low-pressure systems, respectively: AH refers to the Azores High, WEH to the West European High, and IL to the Icelandic Low. The red box over the North Sea highlights regions of enhanced MHWCI.~~ Red upward and blue downward arrows represent increases and decreases in the associated variables. Blue cloud shapes denote cloud cover (CC), while red circles denote geopotential (GP)~~white cloud shapes represent precipitation (Pre)~~. Q_{sw} indicates the downward shortwave heat flux. Green arrows mark horizontal flow convergence or the Meridional Overturning Circulation (MOC).

~~**Appendices A: Validation of SST Data**~~

~~In Sect. 2.1, The high-resolution SST data from OSTIA (Good et al., 2020) is validated by the FerryBox (Macovei et al., 2021), which was developed by Helmholtz-Zentrum Hereon. The FerryBox, installed on commercial vessels, records measurements every 20 seconds along fixed routes, providing data at approximately 100-meter spatial resolution. Our validation is focused on two specific routes: "Hafnia20160120" (0.2°W-8.7°E, 52.6-54.9°N) and "Lysbris20170407" (0.2°W-12.8°E, 51.3-59.4°N). Figure A1 shows high consistency between these two datasets with root mean square error (RMSE) of 0.7 and 1.3 degrees for the year 2016 and 2017, respectively.~~

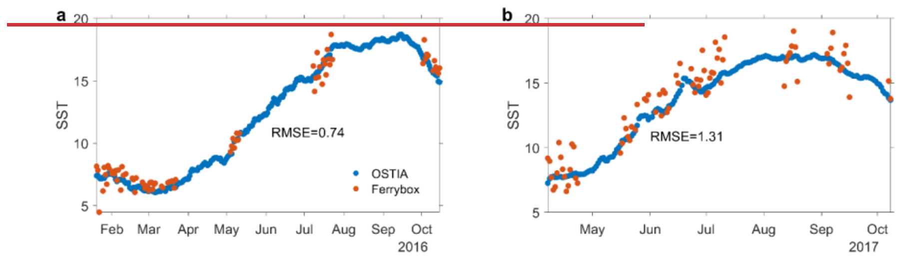

~~**Figure. A1.** Comparison of SST from the Operational Sea Surface Temperature and Sea Ice Analysis (OSTIA) dataset (blue line) with FerryBox in-situ measurements (red dots). Our validation focused on two specific routes: (a) "Hafnia20160120" (0.2°W-8.7°E, 52.6-54.9°N) and (b) "Lysbris20170407" (0.2°W-12.8°E, 51.3-59.4°N).~~

Appendices ~~B~~A: Clustering validation

The stability and interpretability of the correlation-based K-means clustering results were assessed through two complementary analyses: the elbow method and the silhouette coefficient. The elbow curve method runs k-means clustering on the dataset for a range of *K* (from 1 to 10). For each of the *K* values, the total within-cluster sum of squared correlation distances (WCSS) (Lloyd, 1982) was computed. The optimal *K* corresponds to the point at which the decrease in distance becomes substantially less pronounced, indicating that further partitioning does not significantly improve intra-cluster cohesion. As shown in Figure B1, the elbow occurs at $K = 2$, suggesting that two clusters sufficiently capture the dominant spatial patterns of MHWCI variability in the region.

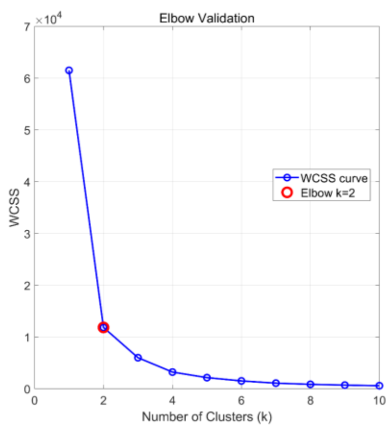

Figure. ~~B1~~A1. Elbow method validation of K-means clustering of marine heatwave cumulative intensity (MHWCI) in the North Sea. The within-cluster sum of squared correlation distances (WCSS) is shown as a function of cluster numbers. The red circle indicates the optimal number of clusters determined by the Elbow method. WCSS denotes the within-cluster sum of squared correlation distances and is a dimensionless clustering metric.

The mean silhouette coefficient (Rousseeuw, 1987) was then calculated for each K using the same correlation distance metric. For a given observation i, the silhouette coefficient is defined as:

$$S(i) = \frac{b(i) - a(i)}{\max\{a(i), b(i)\}}, \quad (4)$$

where $a(i)$ is the average correlation distance between a point and all others in its own cluster, $b(i)$ is the minimum average distance to points in another cluster. The silhouette coefficient ranges from -1 to +1, with higher values indicating better separation. It yielded a favorable score of 0.563 for k = 2, confirming the stability and physical interpretability of the two-cluster partition.

Code availability

The code used for data analysis and visualization in this study is available at Zenodo with DOI: https://doi.org/10.5281/zenodo.17358865

Data availability

All datasets are publicly available. Observational temperature datasets from OSTIA (Worsfold et al., 2024) ~~(Worsfold et al., 2024)~~ were used in this manuscript, available at: https://doi.org/10.48670/moi-00168. The Ferrybox data (Macovei et al., 2021)~~(V. Macovei et al., 2021; V. A. Macovei et al., 2021)~~ are available at https://doi.pangaea.de/10.1594/PANGAEA.930383. The ERA5 (Hersbach, 2023) and ORAS5 (Copernicus Climate Change Service, 2021) are provided by the Copernicus Climate Change Service, available at: https://cds.climate.copernicus.eu/datasets/reanalysis-era5-single-levels-monthly-means?tab=overview and https://cds.climate.copernicus.eu/datasets/reanalysis-oras5?tab=overview.

Author contribution

Y.L. and W.Z. conceived the study together. Y.L. analyzed data and wrote the original draft under the supervision of W.Z. Z.L., Z.F., Q.M., and W.Z. contributed to the revision of the text and helped to determine the final structure of the article.

Competing interests

The authors declare that they have no conflict of interest.

Disclaimer

Publisher's note: Copernicus Publications remains neutral ~~with regard to~~about jurisdictional claims made in the text, published maps, institutional affiliations, or any other geographical representation in this paper. While Copernicus Publications makes every effort to include appropriate place names, the final responsibility lies with the authors.

Acknowledgments

The authors would like to thank Dr. Yoanna Voynova and Dr. Vlad-Alexandru Macovei from Helmholtz-Zentrum Hereon for providing information of the FerryBox installed on commercial vessels travelling in the North Sea.

Financial support

This study is a contribution to the BMBF MARE:N project 'Natural hazards and marine ECOsystem response - causal linkage and predictability (NECO)' (03F0950A: Y.L., W.Z.). It is also supported by the Helmholtz research programme in PoF IV 'Changing Earth—Sustaining our Future'—'Topic 4: Coastal Transition Zones under Natural and Human Pressure' (W.Z.). This work is also supported by a grant from the Research Grants Council of the Hong Kong Special Administrative Region, China (Project Reference Number: AoE/P-601/23-N) and the National Natural Science Foundation of China (Grant numbers: 42230404 and U23A2023). Y.L. is supported by grants from the China Scholarship Council.

References

Allen, E. A., Damaraju, E., Plis, S. M., Erhardt, E. B., Eichele, T., & Calhoun, V. D. (2014). Tracking whole-brain connectivity dynamics in the resting state. *Cereb Cortex*, *24*(3), 663-676. https://doi.org/10.1093/cercor/bhs352

Ardilouze, C., Batté, L., Bunzel, F., Decremer, D., Déqué, M., Doblas-Reyes, F. J., Douville, H., Fereday, D., Guemas, V., MacLachlan, C., Müller, W., & Prodhomme, C. (2017). Multi-model assessment of the impact of soil moisture initialization on mid-latitude summer predictability. *Climate Dynamics*, *49*(11), 3959-3974. https://doi.org/10.1007/s00382-017-3555-7

Artana, C., Rodrigues, R. R., Fevrier, J., & Coll, M. (2024). Characteristics and drivers of marine heatwaves in the western South Atlantic. *Communications Earth & Environment*, *5*(1), 555. https://doi.org/10.1038/s43247-024-01726-8

Börgel, F., Frauen, C., Neumann, T., & Meier, M. (2020). The Atlantic Multidecadal Oscillation controls the impact of the North Atlantic Oscillation on North European climate. *Environmental Research Letters*, *15*. https://doi.org/10.1088/1748-9326/aba925

Brönnimann, S. (2007). Impact of El Niño–Southern Oscillation on European climate. *Reviews of Geophysics*, *45*(3). https://doi.org/https://doi.org/10.1029/2006RG000199

Chauhan, A., Smith, P., Rodrigues, F., Christensen, A., John, M., & Mariani, P. (2023). Distribution and impacts of long-lasting marine heat waves on phytoplankton biomass. *Frontiers in Marine Science*, *10*. https://doi.org/10.3389/fmars.2023.1177571

Chen, S., Chen, W., Wu, R., Yu, B., Graf, H.-F., Cai, Q., Ying, J., & Xing, W. (2025). Atlantic multidecadal variability controls Arctic-ENSO connection. *npj Climate and Atmospheric Science*, *8*(1), 44. https://doi.org/10.1038/s41612-025-00936-x

Chen, W., & Staneva, J. (2024). Characteristics and trends of marine heatwaves in the northwest European Shelf and the impacts on density stratification. *8th edition of the Copernicus Ocean State Report (OSR8)*, *4-osr8*, 7. https://doi.org/10.5194/sp-4-osr8-7-2024

Chen, W., Staneva, J., Grayek, S., Schulz-Stellenfleth, J., & Greinert, J. (2022). The role of heat wave events in the occurrence and persistence of thermal stratification in the southern North Sea. *Nat. Hazards Earth Syst. Sci.*, *22*(5), 1683-1698. https://doi.org/10.5194/nhess-22-1683-2022

Copernicus Climate Change Service, C. D. S. (2021). *ORAS5 global ocean reanalysis monthly data from 1958 to present* (https://doi.org/10.24381/cds.67e8eeb7

de Boisséson, E., & Balmaseda, M. A. (2024). Predictability of marine heatwaves: assessment based on the ECMWF seasonal forecast system. *Ocean Sci.*, *20*(1), 265-278. https://doi.org/10.5194/os-20-265-2024

Delworth, T. L., & Zeng, F. (2016). The Impact of the North Atlantic Oscillation on Climate through Its Influence on the Atlantic Meridional Overturning Circulation. *Journal of Climate*, *29*(3), 941-962. https://doi.org/https://doi.org/10.1175/JCLI-D-15-0396.1

Delworth, T. L., Zeng, F., Zhang, L., Zhang, R., Vecchi, G. A., & Yang, X. (2017). The Central Role of Ocean Dynamics in Connecting the North Atlantic Oscillation to the Extratropical Component of the Atlantic Multidecadal Oscillation. *Journal of Climate*, *30*(10), 3789-3805. https://doi.org/https://doi.org/10.1175/JCLI-D-16-0358.1

Deng, Y., Liu, Z., Zu, T., Hu, J., Gan, J., Lin, Y., Li, Z., Quan, Q., & Cai, Z. (2022). Climatic Controls on the Interannual Variability of Shelf Circulation in the Northern South China Sea. *Journal of Geophysical Research: Oceans*, *127*(7), e2022JC018419. https://doi.org/https://doi.org/10.1029/2022JC018419

England, M. H., Li, Z., Huguenin, M. F., Kiss, A. E., Sen Gupta, A., Holmes, R. M., & Rahmstorf, S. (2025). Drivers of the extreme North Atlantic marine heatwave during 2023. *Nature*, *642*(8068), 636-643. https://doi.org/10.1038/s41586-025-08903-5

Frajka-Williams, E., Beaulieu, C., & Duchez, A. (2017). Emerging negative Atlantic Multidecadal Oscillation index in spite of warm subtropics. *Scientific Reports*, *7*(1), 11224. https://doi.org/10.1038/s41598-017-11046-x

Gröger, M., Dutheil, C., Börgel, F., & Meier, M. H. E. (2024). Drivers of marine heatwaves in a stratified marginal sea. *Climate Dynamics*, *62*(5), 3231-3243. https://doi.org/10.1007/s00382-023-07062-5

Hamdeno, M., Alvera-Azcárate, A., Krokos, G., & Hoteit, I. (2024). Marine Heatwaves in the Red Sea and their Relationship to Different Climate Modes: A Case Study of the 2010 Events in the Northern Red Sea. *EGUsphere*, *2024*, 1-30. https://doi.org/10.5194/egusphere-2024-355

Hansen, F., Feser, F., and Zorita, E. (2024, 14–19 Apr 2024). *Day- and nighttime heatwave clusters over Europe and their physical drivers* EGU General Assembly 2024, Vienna, Austria. https://doi.org/10.5194/egusphere-egu24-16462

Hersbach, H., Bell, B., Berrisford, P., Hirahara, S., Horányi, A., Muñoz Sabater, J., Nicolas, J., Peubey, C., Radu, R., Schepers, D., Simmons, A., Soci, C., Abdalla, S., Abellan, X., Balsamo, G., Bechtold, P., Biavati, G., Bidlot, J., Bonavita, M., & Thépaut, J. N. (2020). The ERA5 global reanalysis. *Quarterly Journal of the Royal Meteorological Society*, *146*. https://doi.org/10.1002/qj.3803

Hersbach, H., Bell, B., Berrisford, P., Biavati, G., Horányi, A., Muñoz Sabater, J., Nicolas, J., Peubey, C., Radu, R., Rozum, I., Schepers, D., Simmons, A., Soci, C., Dee, D., Thépaut, J-N. (2023). *ERA5 monthly averaged data on single levels from 1940 to present* (https://doi.org/10.24381/cds.f17050d7

Hobday, A. J., Alexander, L. V., Perkins, S. E., Smale, D. A., Straub, S. C., Oliver, E. C. J., Benthuysen, J. A., Burrows, M. T., Donat, M. G., Feng, M., Holbrook, N. J., Moore, P. J., Scannell, H. A., Sen Gupta, A., & Wernberg, T. (2016). A hierarchical approach to defining marine heatwaves. *Progress in Oceanography*, *141*, 227-238. https://doi.org/https://doi.org/10.1016/j.pocean.2015.12.014

Hobday, A. J., & Pecl, G. T. (2014). Identification of global marine hotspots: sentinels for change and vanguards for adaptation action. *Reviews in Fish Biology and Fisheries*, *24*(2), 415-425. https://doi.org/10.1007/s11160-013-9326-6

Holbrook, N. J., Scannell, H. A., Sen Gupta, A., Benthuysen, J. A., Feng, M., Oliver, E. C. J., Alexander, L. V., Burrows, M. T., Donat, M. G., Hobday, A. J., Moore, P. J., Perkins-Kirkpatrick, S. E., Smale, D. A., Straub, S. C., & Wernberg, T. (2019). A global assessment of marine heatwaves and their drivers. *Nature Communications*, *10*(1), 2624. https://doi.org/10.1038/s41467-019-10206-z

Hou, J., Fang, Z., & Geng, X. (2023). Recent Strengthening of the ENSO Influence on the Early Winter East Atlantic Pattern. *Atmosphere*, *14*(12), 1809. https://www.mdpi.com/2073-4433/14/12/1809

Jacox, M. G., Alexander, M. A., Amaya, D., Becker, E., Bograd, S. J., Brodie, S., Hazen, E. L., Pozo Buil, M., & Tommasi, D. (2022). Global seasonal forecasts of marine heatwaves. *Nature*, *604*(7906), 486-490. https://doi.org/10.1038/s41586-022-04573-9

Jain, A. K. (2010). Data clustering: 50 years beyond K-means. *Pattern Recognition Letters*, *31*(8), 651-666. https://doi.org/https://doi.org/10.1016/j.patrec.2009.09.011

Jiménez-Esteve, B., & Domeisen, D. I. V. (2018). The Tropospheric Pathway of the ENSO–North Atlantic Teleconnection. *Journal of Climate*, *31*(11), 4563-4584. https://doi.org/https://doi.org/10.1175/JCLI-D-17-0716.1

Josey, S. A., & Sinha, B. (2022). Subpolar Atlantic Ocean mixed layer heat content variability is increasingly driven by an active ocean. *Communications Earth & Environment*, *3*(1), 111. https://doi.org/10.1038/s43247-022-00433-6

Kerr, R. A. (2000). A North Atlantic Climate Pacemaker for the Centuries. *Science*, *288*(5473), 1984-1985. https://doi.org/doi:10.1126/science.288.5473.1984

Lin, Y.-F., Terng, C.-T., Wu, C.-R., & Yu, J.-Y. (2023). Seasonally-reversed trends in the subtropical Northwestern Pacific linked to asymmetric AMO influences. *Scientific Reports*, *13*(1), 13735. https://doi.org/10.1038/s41598-023-40979-9

Liu, K., Xu, K., Zhu, C., & Liu, B. (2022). Diversity of Marine Heatwaves in the South China Sea Regulated by ENSO Phase. *Journal of Climate*, *35*(2), 877-893. https://doi.org/https://doi.org/10.1175/JCLI-D-21-0309.1

Liu, Q. Y., Wang, D., Wang, X., Shu, Y., Xie, Q., Chen, J., Liu, Q. Y., Wang, D., Wang, X., & Shu, Y. (2014). Thermal variations in the South China Sea associated with the eastern and central Pacific El Nino events and their mechanisms. *Journal of Geophysical Research Oceans*, *119*(12), 8955-8972.

Lloyd, S. (1982). Least squares quantization in PCM. *IEEE Transactions on Information Theory*, *28*(2), 129-137. https://doi.org/10.1109/TIT.1982.1056489

Loganantharaj, R., Cheepala, S., & Clifford, J. (2006). Metric for measuring the effectiveness of clustering of DNA microarray expression. *BMC Bioinformatics*, *7 Suppl 2*(Suppl 2), S5. https://doi.org/10.1186/1471-2105-7-s2-s5

Macovei, V., Voynova, Y., Gehrung, M., & Petersen, W. (2021). Ship-of-Opportunity, FerryBox-integrated, membrane-based sensor pCO2, temperature and salinity measurements in the surface North Sea since 2013. *PANGAEA*.
Marin, M., Feng, M., Phillips, H. E., & Bindoff, N. L. (2021). A Global, Multiproduct Analysis of Coastal Marine Heatwaves: Distribution, Characteristics, and Long-Term Trends. *Journal of Geophysical Research: Oceans*, *126*(2), e2020JC016708. https://doi.org/https://doi.org/10.1029/2020JC016708
Mathis, M., & Pohlmann, T. (2014). Projection of physical conditions in the North Sea for the 21st century. *Climate Research*, *61*, 1-17. https://doi.org/10.3354/cr01232
McAdam, R., Masina, S., & Gualdi, S. (2023). Seasonal forecasting of subsurface marine heatwaves. *Communications Earth & Environment*, *4*(1), 225. https://doi.org/10.1038/s43247-023-00892-5
Mi, C., Yi, A., Xue, J., Dong, C., & Shan, H. (2025). Forecasting summer marine heatwaves in the South China Sea using explainable machine learning models. *Deep Sea Research Part I: Oceanographic Research Papers*, *218*, 104457. https://doi.org/https://doi.org/10.1016/j.dsr.2025.104457
Moat, B. I., Smeed, D. A., Frajka-Williams, E., Desbruyères, D. G., Beaulieu, C., Johns, W. E., Rayner, D., Sanchez-Franks, A., Baringer, M. O., Volkov, D., Jackson, L. C., & Bryden, H. L. (2020). Pending recovery in the strength of the meridional overturning circulation at 26° N. *Ocean Sci.*, *16*(4), 863-874. https://doi.org/10.5194/os-16-863-2020
Mohamed, B., Barth, A., & Alvera-Azcárate, A. (2023). Extreme marine heatwaves and cold-spells events in the Southern North Sea: classifications, patterns, and trends. *Frontiers in Marine Science*, *10*, Article 1258117. https://doi.org/10.3389/fmars.2023.1258117
Mohamed, B., Barth, A., & Alvera-Azcárate, A. (2024). *The summer marine heatwaves in the North Sea in 2023*. https://doi.org/10.5194/egusphere-egu24-8900
Mohamed, B., Barth, A., Van der Zande, D., & Alvera-Azcárate, A. (2025). Amplified warming and marine heatwaves in the North Sea under a warming climate and their impacts. *Ocean Sci.*, *21*(5), 2505-2525. https://doi.org/10.5194/os-21-2505-2025
Mohamed, B., Ibrahim, O., & Nagy, H. (2022). Sea Surface Temperature Variability and Marine Heatwaves in the Black Sea. *Remote Sensing*, *14*(10), 2383. https://www.mdpi.com/2072-4292/14/10/2383
Mooney, C. (2015). *Why some scientists are worried about a cold 'blob' in the North Atlantic ocean. Washington Post* https://www.washingtonpost.com/news/energy-environment/wp/2015/09/24/why-some-scientists-are-worried-about-a-cold-blob-in-the-north-atlantic-ocean/?utm%20term=.24388ab9clec
Oliver, E. C. J., Donat, M. G., Burrows, M. T., Moore, P. J., Smale, D. A., Alexander, L. V., Benthuysen, J. A., Feng, M., Sen Gupta, A., Hobday, A. J., Holbrook, N. J., Perkins-Kirkpatrick, S. E., Scannell, H. A., Straub, S. C., & Wernberg, T. (2018). Longer and more frequent marine heatwaves over the past century. *Nature Communications*, *9*(1), 1324. https://doi.org/10.1038/s41467-018-03732-9
Oliver, E. C. J., Perkins-Kirkpatrick, S. E., Holbrook, N. J., & Bindoff, N. L. (2018). Anthropogenic and Natural Influences on Record 2016 Marine Heat waves. *Bulletin of the American Meteorological Society*, *99*(1), S44-S48. https://doi.org/https://doi.org/10.1175/BAMS-D-17-0093.1
Oshika, M., Tachibana, Y., & Nakamura, T. (2015). Impact of the winter North Atlantic Oscillation (NAO) on the Western Pacific (WP) pattern in the following winter through Arctic sea ice and ENSO: part I—observational evidence. *Climate Dynamics*, *45*(5), 1355-1366. https://doi.org/10.1007/s00382-014-2384-1
Patterson, M., Weisheimer, A., Befort, D. J., & O'Reilly, C. H. (2022). The strong role of external forcing in seasonal forecasts of European summer temperature. *Environmental Research Letters*, *17*(10), 104033. https://doi.org/10.1088/1748-9326/ac9243
Pearce, A., Lenanton, R., Jackson, G., Moore, J., Feng, M., & Gaughan, D. (2011). *The 'marine heat wave' off Western Australia during the summer of 2010/11*. (978-1-921845-25-3). Western Australia Department of Fisheries
Podesta, G., & Glynn, P. (2001). The 1997-98 El Niño event in Panama and Galápagos: An update of thermal stress indices relative to coral bleaching. *Bulletin of Marine Science*, *69*, 43-59.
Quante, M., & Colijn, F. (2016). *North Sea Region Climate Change Assessment*. Springer International Publishing : Imprint : Springer. https://doi.org/10.1007/978-3-319-39745-0
Rousseeuw, P. J. (1987). Silhouettes: A graphical aid to the interpretation and validation of cluster analysis. *Journal of Computational and Applied Mathematics*, *20*, 53-65. https://doi.org/https://doi.org/10.1016/0377-0427(87)90125-7
Scaife, A. A., Dunstone, N., Hardiman, S., Ineson, S., Li, C., Lu, R., Pang, B., Klein-Tank, A., Smith, D., Van Niekerk, A., Renwick, J., & Williams, N. (2024). ENSO affects the North Atlantic Oscillation 1 year later. *Science*, *386*(6717), 82-86. https://doi.org/doi:10.1126/science.adk4671

Scannell, H. A., Pershing, A. J., Alexander, M. A., Thomas, A. C., & Mills, K. E. (2016). Frequency of marine heatwaves in the North Atlantic and North Pacific since 1950. *Geophysical Research Letters*, *43*(5), 2069-2076. https://doi.org/https://doi.org/10.1002/2015GL067308

Shackelford, K., DeMott, C. A., van Leeuwen, P. J., & Barnes, E. A. (2025). A Regimes-Based Approach to Identifying Seasonal State-Dependent Prediction Skill. *Journal of Geophysical Research: Atmospheres*, *130*(8), e2024JD042917. https://doi.org/https://doi.org/10.1029/2024JD042917

Sun, C., Li, J., & Jin, F.-F. (2015). A delayed oscillator model for the quasi-periodic multidecadal variability of the NAO. *Climate Dynamics*, *45*(7), 2083-2099. https://doi.org/10.1007/s00382-014-2459-z

Syakur, M. A., Khotimah, B. K., Rochman, E. M. S., & Satoto, B. D. (2018). Integration K-Means Clustering Method and Elbow Method For Identification of The Best Customer Profile Cluster. *IOP Conference Series: Materials Science and Engineering*, *336*(1), 012017. https://doi.org/10.1088/1757-899X/336/1/012017

Takaya, K., & Nakamura, H. (2001). A Formulation of a Phase-Independent Wave-Activity Flux for Stationary and Migratory Quasigeostrophic Eddies on a Zonally Varying Basic Flow. *Journal of the Atmospheric Sciences*, *58*(6), 608-627. https://doi.org/https://doi.org/10.1175/1520-0469(2001)058<0608:AFOAPI>2.0.CO;2

Tan, W., Wang, X., Wang, W., Wang, C., & Zuo, J. (2016). Different Responses of Sea Surface Temperature in the South China Sea to Various El Niño Events during Boreal Autumn. *Journal of Climate*, *29*(3), 1127-1142.

Thornton, H. E., Smith, D. M., Scaife, A. A., & Dunstone, N. J. (2023). Seasonal Predictability of the East Atlantic Pattern in Late Autumn and Early Winter. *Geophysical Research Letters*, *50*(1), e2022GL100712. https://doi.org/https://doi.org/10.1029/2022GL100712

Trenberth, K. E., & Shea, D. J. (2006). Atlantic hurricanes and natural variability in 2005. *Geophysical Research Letters*, *33*(12). https://doi.org/https://doi.org/10.1029/2006GL026894

van der Molen, J., & Pätsch, J. (2022). An overview of Atlantic forcing of the North Sea with focus on oceanography and biogeochemistry. *Journal of Sea Research*, *189*, 102281. https://doi.org/https://doi.org/10.1016/j.seares.2022.102281

Vivekanandan, E., Ali, M. H., Jasper, B., Rajagopalan, M., & Marine, C. (2008). Thermal thresholds for coral bleaching in the Indian seas.

Vogt, L., Burger, F., Griffies, S., & Frölicher, T. (2022). Local Drivers of Marine Heatwaves: A Global Analysis With an Earth System Model. *Frontiers in Climate*, *4*. https://doi.org/10.3389/fclim.2022.847995

Wang, Y., & Zhou, Y. (2024). Seasonal dynamics of global marine heatwaves over the last four decades. *Frontiers in Marine Science*, *11*. https://doi.org/10.3389/fmars.2024.1406416

Wicker, W., Harnik, N., Pyrina, M., & Domeisen, D. I. V. (2024). Heatwave Location Changes in Relation to Rossby Wave Phase Speed. *Geophysical Research Letters*, *51*(14), e2024GL108159. https://doi.org/https://doi.org/10.1029/2024GL108159

Woollings, T., Barriopedro, D., Methven, J., Son, S.-W., Martius, O., Harvey, B., Sillmann, J., Lupo, A. R., & Seneviratne, S. (2018). Blocking and its Response to Climate Change. *Current Climate Change Reports*, *4*(3), 287-300. https://doi.org/10.1007/s40641-018-0108-z

Worsfold, M., Good, S., Atkinson, C., & Embury, O. (2024). Presenting a Long-Term, Reprocessed Dataset of Global Sea Surface Temperature Produced Using the OSTIA System. *Remote Sensing*, *16*(18), 3358. https://www.mdpi.com/2072-4292/16/18/3358

Xue, J., Zhang, W., Zhang, Y., Luo, J.-J., Zhu, H., Sun, C., & Yamagata, T. (2025). Interdecadal modulation of Ningaloo Niño/Niña strength in the Southeast Indian Ocean by the Atlantic Multidecadal Oscillation. *Nature Communications*, *16*(1), 1966. https://doi.org/10.1038/s41467-025-57160-7

Yan, Y., Chai, F., Xue, H., & Wang, G. (2020). Record-Breaking Sea Surface Temperatures in the Yellow and East China Seas. *Journal of Geophysical Research: Oceans*, *125*(8), e2019JC015883. https://doi.org/https://doi.org/10.1029/2019JC015883

Zhao, Z., & Marin, M. (2019). A MATLAB toolbox to detect and analyze marine heatwaves Software. *Journal of Open Source Software*, *4*. https://doi.org/10.21105/joss.01124

Zuo, H., Balmaseda, M. A., Tietsche, S., Mogensen, K., & Mayer, M. (2019). The ECMWF operational ensemble reanalysis–analysis system for ocean and sea ice: a description of the system and assessment. *Ocean Sci.*, *15*(3), 779-808. https://doi.org/10.5194/os-15-779-2019